



TECHNICAL UNIVERSITY OF DENMARK

DYNAMICS OF MACHINERY
41514

Report 2

Author:
Christian Casarotto (s223302)

Instructor:
Prof. Ilmar Santos

May 13, 2023

Contents

Introduction

1	Modelling the Lateral Dynamics of the Shaft	1
1.1	Assumptions and theory	1
1.2	Shaft models	3
1.3	Validation and model refinements	4
2	Modeling the Lateral Dynamics of Shaft and Discs	5
2.1	One disk model	6
2.2	Two disks model	8
3	Modelling the Ball Bearing and Coupling	9
3.1	Bearing stiffness influence study	10
3.2	Prediction of Critical Speeds Using Two Ball Bearings	11
3.3	Unbalance Response Using Two Ball Bearings	13
4	Modelling the Hydrodynamic Bearing and Coupling	14
4.1	Static and Dynamic Properties	15
4.2	Prediction of critical speeds and stability limit	17
4.3	Unbalance response	19
4.4	Engineering Design	20
	List of Figures	I
	List of Tables	II
	References	II
5	Appendix	III

Introduction

Most of the energy in the planet is produced by rotating machines, from nuclear power plants to hydroelectric turbines, making them a topic of high interest in machine dynamics and vibrations. For these machines it is important to predict critical speeds, stability threshold, vibration amplitude and other parameters within the machine speed range.

The aim of this document is to analyze a large overhung centrifugal compressor, understanding how real and imaginary parts of eigenvalues and eigenvectors change as a function of the operational speeds. The compressor is composed of a large shaft and two impellers, constituted by disks of different thickness.

The document is divided in four main chapters. In the first part the mechanical and mathematical models of the flexible shaft is obtained by Finite Element Method (FEM). In the second chapter the models are expanded to include the disk (impeller). Partial data is used to validate and adjust the finite element models, which are expanded in the third and fourth chapter to include the bearing. Chapter three considers a ball bearing and chapter four a journal bearing, with final considerations on the influence and characteristic of different types of bearing.

1 Modelling the Lateral Dynamics of the Shaft

The first step in the project is to obtain a simple mechanical model of the shaft of the compressor, to study the lateral vibrations. In this phase the shaft is in a free-free condition, so without bearings or discs attached, and the angular velocity is of course zero ($\Omega = 0$). The drawings are available in the pdf assignment.

1.1 Assumptions and theory

The finite element method (FEM) is used to study the lateral vibrations of the shaft. The shaft is divided into finite elements, each with four degrees of freedom at each extremity: $q = [v, w, \beta, \Gamma]$ representing translations along y and z and rotations around y and z . This yields eight degrees of freedom for the full element, as shown in figure 1.

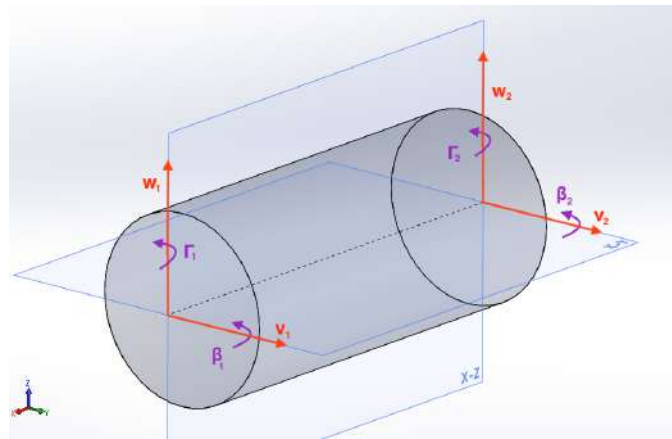


Figure 1: Shaft element with degrees of freedom

The modelling technique used in the analysis is based on Lagrange equation (1.1). In this equation kinetic and potential energy of the element are expressed as function of the degrees of freedom, $E_{kin} = f(q)$ and $E_{pot} = f(q)$, and derived with respect to q , where n_{dof} is the number of degrees of freedom, i.e. eight for the shaft element.

$$\frac{d}{dt} \left(\frac{\partial E_{kin}}{\partial \dot{q}_i} \right) - \frac{\partial E_{kin}}{\partial q_i} + \frac{\partial E_{pot}}{\partial q_i} = F_i \quad i = (1, \dots, n_{dof}) \quad (1.1)$$

Here \dot{q}_i is the derivative of the degrees of freedom, the velocities $\dot{q} = [\dot{v}, \dot{w}, \dot{\beta}, \dot{\Gamma}]$. From equation 1.1 one gets the generalized forces F_i , yielding to n_{dof} generalized equations, so eight equations for each shaft element.

Some assumptions are needed to treat the shaft elements and obtain its E_{kin} and E_{pot} . Specifically each element is considered having distributed mass and studied as a Euler-Bernoulli beam. This excludes shear forces on the element but allows for deflections. Moreover damping is assumed to be null in the shaft and will only be considered in the hydrodynamic bearings, as described in chapter 4. The potential energy of each element can be seen as the energy stored in its deformation and the deflection shape can be approximated by knowing the movements of the extremities. This is done using linear shape functions that express translation and rotation as function of degrees of

freedom. Depending on which degree of freedom is activated, translation $\psi(x')$ and rotation $\theta(x')$ at a given local coordinate of the element x' are expressed with one of the equations in appendix A (5), of which an example is reported in equation 1.2.

$$\psi_1(x') = 1 - \frac{3}{l^2}x'^2 + \frac{2}{l^3}x'^3 \quad \theta_1(x') = \dot{\psi}_1(x') = -\frac{6}{l^2}x' + \frac{6}{l^3}x'^2 \quad (1.2)$$

For each shaft element the degrees of freedom can be expressed as in equation 1.3 and the shape functions in matrix form. The shape functions are multiplied by the degrees of freedom, giving translations and rotations of the element at a given coordinate x' and in time t , as q changes in time. All this process is described in appendix A (5) in detail.

Once obtained the vectors V , W , β and Γ , describing the translations and rotations, its easy to find velocities and accelerations by simple derivation. The potential energy is found with the integral in equation 1.7, which becomes the stiffness matrix due to bending of the system, K_b . Similarly happens with the kinetic energy, yielding mass matrix due to translations and rotations M_T and M_R and gyroscopic matrix G , as from equations 1.4 to 1.6. See appendix for details on Ψ and Θ functions.

$$q(t) = [v_1, w_1, \beta_1, \Gamma_1, v_2, w_2, \beta_2, \Gamma_2]^T \quad (1.3)$$

$$M_T = \int_0^l \mu \cdot \Psi^T \cdot \Psi dx' \quad (1.4)$$

$$M_R = \int_0^l I_d \cdot \Theta^T \cdot \Theta dx' \quad (1.5)$$

$$G_S = \int_0^l I_p \cdot \Theta_\Gamma^T \cdot \Theta_\beta dx' \quad (1.6)$$

$$K_B = \int_0^l EI \cdot \ddot{\Psi}^T \cdot \ddot{\Psi} dx' \quad (1.7)$$

Density of the material μ can be left outside the integral as constant, I , I_d and I_p are the moments of inertia of the element. The resulting 8x8 matrices for each portion of shaft are obtained and collected in appendix A (5) due to space constrain. All matrices are symmetric beside the gyroscopic matrix G_S , which is anti-symmetric, so $G_S = -G_S^T$. As the elements are not considered simple particles, the mass matrices are not diagonal, but the mass is already distributed in the matrix trough the shape functions.

$$(M_T + M_R) \cdot \ddot{q} - \Omega \cdot G_S \cdot \dot{q} + K_B \cdot q = F \quad (1.8)$$

With the obtained matrices it is possible to rewrite the system of eight equations from Lagrange as in 1.8, where the degrees of freedom q is the vector in 1.3, expressed for the two nodes. The \dot{q} and \ddot{q} derivatives are velocities and accelerations and F is the vector of generalized forces. For the shaft model validation the velocity is considered as zero, so the equations reduce to only mass and stiffness matrices.

From equation 1.8, one can find eigenvector U and eigenvalues λ with equation 1.11, where the M_{glob} and K_{glob} matrices are given in 1.9 and 1.10. This can be taken as a general procedure to get U and λ , which will be used thought all the document. In this shaft only model speed Ω and damping matrix D are of course 0.

$$M_{\text{glob}} = \begin{bmatrix} M & 0 \\ 0 & M \end{bmatrix} \quad (1.9) \quad K_{\text{glob}} = \begin{bmatrix} -G \cdot \Omega + D & K \\ -M & 0 \end{bmatrix} \quad (1.10)$$

$$[U, \lambda] = \text{eig}(-K_{\text{glob}}, M_{\text{glob}}) \quad (1.11)$$

1.2 Shaft models

In creating a FEM model, balancing accuracy and computational efficiency is crucial. In this analysis, the entire length of the shaft provided in the assignment, which is 1150 mm, is considered. However, minor details such as fillet radius and bearing extraction slots are excluded as they have negligible impact on the shaft dynamics and are not relevant for this study.

The FEM model was built using five levels of discretization to perform a convergence study and determine the optimal number and size of elements for accurate results. Initially, the shaft was treated as an equivalent shaft with the same volume as the physical model but a constant diameter. The volume of the shaft was obtained by summing all n sections of different radius (r_i) and length (l_i), from which the equivalent diameter was calculated:

$$\text{Volume} = \pi \sum_{i=1}^n r_i^2 l_i = 6.33e6 \text{ mm}^2 \rightarrow D_{eq} = 83.716 \text{ mm} \quad (1.12)$$

With this D_{eq} five levels of discretization are created, with 5, 10, 15, 20 and 25 elements of constant length and dimensions. These are referred to as model i with $i = 1, \dots, 5$.

Using a modified version of the MatLab code "flexible-rotor-modal-DTU-c.m" it is possible to calculate the undamped natural frequencies and modes shapes of the shaft in a free-free condition and carry out a convergence study. Of course the natural frequencies are taken from the eigenvalues λ , equation 1.11. This study is reported in table 1 where the five models are analyzed.

	# elements	<i>Freq.1</i> [Hz]	<i>Freq.2</i> [Hz]	<i>Freq.3</i> [Hz]	<i>Freq.4</i> [Hz]
Model 1	5	283	775	1510	2462
Model 2	10	283	773	1498	2442
Model 3	15	283	773	1497	2438
Model 4	20	283	773	1496	2437
Model 5	25	283	773	1496	2437

Table 1: Convergence study with five levels of discretization

In this analysis the first natural frequencies associated with rigid body modes were neglected, as part of the low frequency range. Also a small value of stiffness at the edges of the shaft was added to overcome numerical problems in simulating the free-free condition of the shaft. From the table it is evident how 15 - 25 elements give a good approximation, this translates in an element dimension of 45 - 75 mm. The considered frequencies are the ones associated to mode shapes in the vertical plane (X-Z), but as the velocity is null these correspond to the frequencies and mode shapes in the horizontal plane.

1.3 Validation and model refinements

It is now important to validate the model by comparing it with the given experimental data. The results from experimental modal analysis are reported in table 2, together with the natural frequencies obtained from the fifth model and the discrepancy in %.

	<i>Freq.1</i> [Hz]	<i>Freq.2</i> [Hz]	<i>Freq.3</i> [Hz]	<i>Freq.4</i> [Hz]
Experimental	388	930	1689	2624
Model 5	283	773	1496	2437
Discrepancy	27.1 %	16.9 %	11.4 %	7.1 %

Table 2: Discrepancy between experimental natural frequencies and model - shaft only

The initial model using an equivalent diameter was found to be insufficiently accurate in predicting natural frequencies, particularly at low frequencies. A new model was developed, taking into account diameter variations along the shaft. Nodes were placed corresponding to the locations of disks and bearings, and additional nodes were added while maintaining a roughly constant element size. An equivalent diameter was used where necessary. The resulting model consisted of 20 elements and is described in Table 3.

Elements	1	2	3	4-5	6	7-8	9-18	19	20
Length [mm]	65	35	40	50	55	60	62.5	46.5	63.5
Diameter [mm]	54.28	70.00	70.00	70.00	90.00	99.60	90.00	53.27	53.27

Table 3: Final model of the shaft with dimensions, *initial shaft model*

The results given by such model are much better than the previous ones, leading to a discrepancy always below 3% between model and experiments, as illustrated in table 4. The theoretical model created for the shaft is referred to as *initial shaft model* in the rest of the document. Two examples of mode shapes given by this model are presented in figures 2 and 3, after filtering the eigenvectors U obtained in 1.11. To get a better definition of the mode shapes 40 points were used in the graphs.

	<i>Freq.1</i> [Hz]	<i>Freq.2</i> [Hz]	<i>Freq.3</i> [Hz]	<i>Freq.4</i> [Hz]
Theoretical	382	941	1644	2562
Experimental	388	930	1689	2624
Discrepancy	1.5 %	1.2 %	2.7 %	2.4 %

Table 4: Comparison between theoretical model and experiments

For this shaft only model the mode shapes are quite straight forward, mode two and three are collected in appendix B (5), while mode one and four are presented. The system vibrates with an increasing frequency and number of nodes, with great amplitude towards the extremities. Also the overall amplitude reduces with the frequency, and the movements presented are definitely rigid body motions of the shaft.

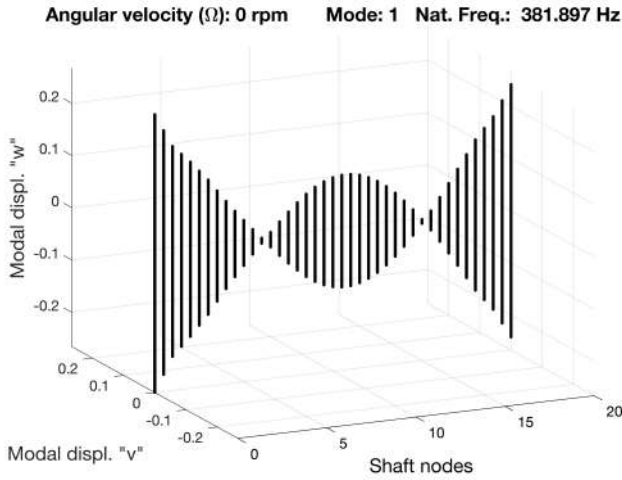


Figure 2: Mode shape 1 - Shaft only

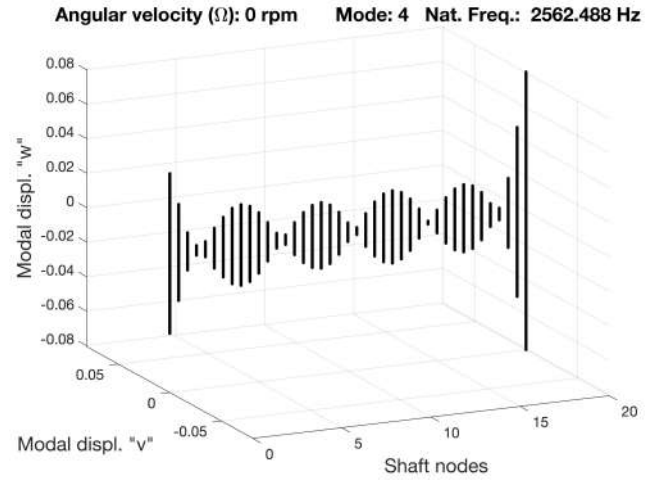


Figure 3: Mode shape 4 - Shaft only

2 Modeling the Lateral Dynamics of Shaft and Discs

The second modelling phase of the centrifugal compressor consists in adding the impellers to the shaft. The impellers are constituted by steel discs, based on the provided technical drawings. The process to create the FEM model of the discs is similar to the one for the shaft, but discs only occupy one node and therefore only have four degrees of freedom. One aims at using again Lagrange equation (1.1) with kinetic and potential energy as function of the degrees of freedom. The disks are assumed to be rigid, so in the analysis no deformations is considered. As E_{pot} is mainly the energy stored in the deformation this is considered null. The kinetic energy to be used in equation 1.1 is given by the absolute speed of the disk, ω . This rotation speed in the summation of the three rotation of the disc around the three axis, $I\dot{\Gamma}$, $B_1\dot{\beta}$ and $B_2\dot{\phi}$. As from equation 2.13 these speed are summed up in the local reference frame B_3 , therefore rotated with the transformation matrices T_ϕ , T_β and T_Γ , made available in appendix A (5). With this absolute velocity in the local reference it is possible to calculate E_{kin} as in equation 2.14.

$${}_{B3}\omega = T_\phi T_\beta T_\Gamma \cdot I\dot{\Gamma} + T_\phi T_\beta \cdot I\dot{\beta} + T_\phi \cdot I\dot{\phi} \quad (2.13)$$

$$E_{kin} = \frac{1}{2} I V^T M_D I V + \frac{1}{2} {}_{B3}\omega^T {}_{B3}I {}_{B3}\omega \quad (2.14)$$

Here M_D and ${}_{B3}I$ are disk mass and inertia matrices. Similarly to the shaft element, obtained E_{kin} as a function of the degrees of freedom, one can complete the Lagrange equation and get a system of in this case four equations. The system is represented in equation 2.15, where mass matrix M for the disk and gyroscopic matrix G_D are in equations 5.38 and 5.39 in the appendix. Differently from the shaft element case M is now diagonal, as the disk is assumed to be infinitely thin, with concentrated mass. G_D is again anti-diagonal, and does not constitute dissipation of energy. In the first part of the analysis the velocity is null, and equation 2.15 reduces to only the first term.

$$M \cdot \ddot{q} - \Omega \cdot G_D \cdot \dot{q} = F \quad (2.15)$$

2.1 One disk model

The first impeller to be assembled is the 100 mm thick one. Several models of increasing complexity were created, to study the effects of geometrical simplifications. These are described in the following list:

1. Model_1_1disc → Shaft: *initial shaft model*. Disk: modelled as a full disk, neglecting the surface channels and considering a $D_{i,eq} = 85.67$ mm as internal diameter.
2. Model_2_1disc → Same as above but considering the channels at the edge of the disk as a single channel in the middle of the disk.
3. Model_3_1disc → Same as above but considering the channels as in the real component, therefore using Steiner's theorem to adjust I_d .
4. Model_4_1disc → Same as the previous model, but the internal diameters of the disk are considered as in reality, and not as an equivalent diameter.
5. Model_5_1disc → Same as in the previous model, but the number of elements of the shaft are doubled, reaching 40 elements of half length.
6. Model_6_1disc → Same as in model 5, but the elements are 22 and rearranged to better fit the real changes in diameter of the shaft.

	Freq.1 [Hz]	Freq.2 [Hz]	Freq.3 [Hz]	Freq.4 [Hz]	Freq.5 [Hz]
Model 1 - 1d	293	605	1275	1797	2315
	2.66 %	9.57 %	5.42 %	9.92 %	2.85 %
Model 2 - 1d	297	618	1280	1811	2318
	1.33 %	7.62 %	5.04 %	9.22 %	2.73 %
Model 3 - 1d	298	618	1280	1812	2318
	1 %	7.62 %	5.04 %	9.17 %	2.73 %
Model 4 - 1d	298	619	1280	1813	2318
	1 %	7.47 %	5.04 %	9.12 %	2.73 %
Model 5 - 1d	298	619	1280	1819	2318
	1 %	7.47 %	5.04 %	8.82 %	2.73 %
Model 6 - 1d	301	626	1319	1925	2481
	0 %	6.43 %	2.15 %	3.51 %	4.11 %
Corrected - 1d	305	640	1323	1940	2483
	1.33 %	4.33 %	1.85 %	2.76 %	4.20 %
Experimental - 1d	301	669	1348	1995	2383

Table 5: One disk - results from all models and discrepancies

The results were compared with the experimental data to verify the quality of the models. The data for each model is in table 5 with the related discrepancies. In the experimental data the 4th

frequency is only visible when exciting at node 6, probably because the other excitation points are close to mode 4 nodes.

Models 1 to 5 were compared, with discrepancies below 5% marked in green and the others in red and orange. Results showed that the greater the distance from the axis, the greater is its influence due to the variation of I_d . Models 4 and 5 gave the same results, confirming the convergence study. However, the second natural frequency of the last model was not in the desired range. By reducing I_d by 10%, all natural frequencies fell below the threshold. The modified model is named *Corrected - 1d*. The mass of the model disk is 45.9 [kg] and the inertia is 0.2962 [kgm²]. Examples of mode shape obtained with the final model are in figure 4 to 7, again using twice the points. Due to space constrain mode shape three is in appendix B (5).

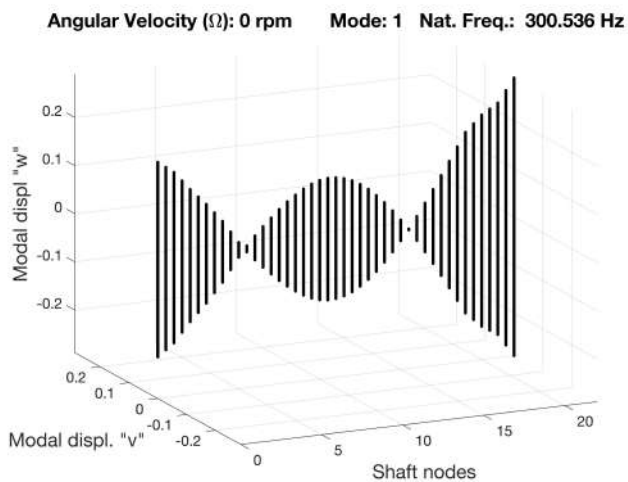


Figure 4: Mode shape 1, Shaft + 1 disk

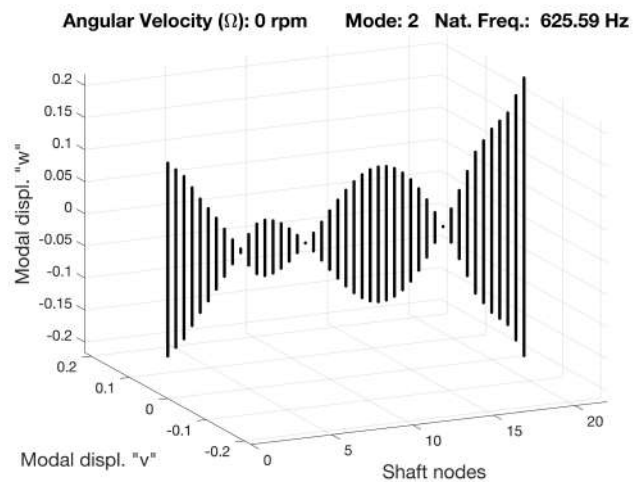


Figure 5: Mode shape 2, Shaft + 1 disk

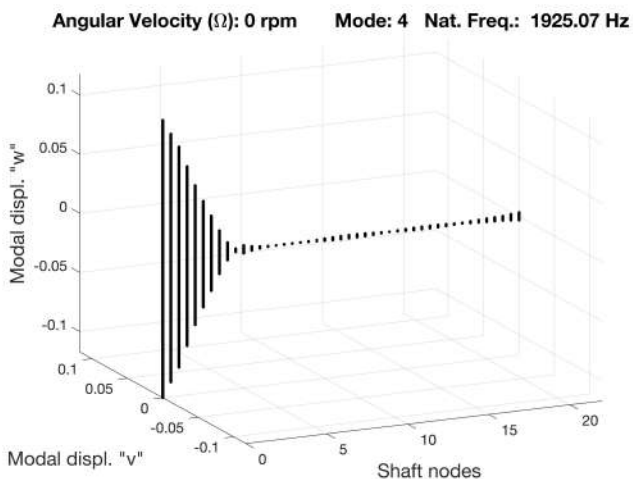


Figure 6: Mode shape 4, Shaft + 1 disk

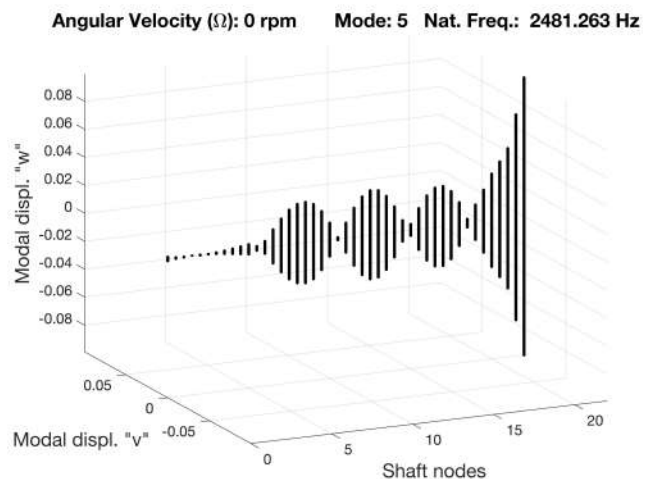


Figure 7: Mode shape 5, Shaft + 1 disk

The mode shapes are similar to the ones presented in section 1.3, but here it is evident the huge influence of the disk. As the system is stationary, the disk mass makes it so that it constitutes a node in the vibration, and the amplitude is moved towards the free sides of the shaft and extremities. The

shaft deflects around the disk, as there is not enough energy to move the disk, and the amplitude again decreases with the frequency.

2.2 Two disks model

The second disk is modeled using the same assumptions as for disk one, so thin and rigid disk with no deformation. Also the geometrical assumptions are similar, yielding to another equation like 2.15 for the second disk.

Starting from the final model of the one disk case, namely *model 6-1d* in table 5, one can extend the model adding the second disk as happened with the first one. This yields to the first model in table 6, for which the discrepancy seem overall good everywhere but for the third one. The other models are:

1. Model_2_2disc \rightarrow Same as *model_1_2disc*, with steel density $\rho = 7850 \text{ kg/m}^3$.
2. Model_3_2disc \rightarrow Same as *model_1_2disc*, with I_d increased of 10% for both disks.
3. Model_4_2disc \rightarrow Fusion of the models above, with increased density and inertia.

	<i>Freq.1</i> [Hz]	<i>Freq.2</i> [Hz]	<i>Freq.3</i> [Hz]	<i>Freq.4</i> [Hz]	<i>Freq.5</i> [Hz]
Model 1 - 2d	237	496	824	1330	2422
	1.66 %	0.4 %	16.38 %	6.4 %	3.06 %
Model 2 - 2d	236	494	821	1325	2414
	2.07 %	0.8 %	15.96 %	6 %	2.72 %
Model 3 - 2d	232	489	793	1323	2399
	3.73 %	1.81 %	12.01 %	5.84 %	2.09 %
Model 4 - 2d	231	487	790	1319	2391
	4.15 %	2.21 %	11.58 %	5.52 %	1.74 %
Experimental - 2d	241	498	708	1250	2350

Table 6: Two disks - results from all models and discrepancies

Despite the modifications it was not possible to lower the third frequency discrepancy below 10%. This is probably due to the model assumptions, especially the thin disk assumption influences the rigidity of the shaft, as the disks are considered concentrated masses despite the large dimensions. In all the disks area the shaft is in reality not free to deflect, due to the bulky presence of the disks. Also the assumption of no damping in the shaft is probably too conservative, as illustrated by the systematically higher last three frequencies.

The final model is *model 4 - 2d*, with increased inertia and steel density, as it was not possible to improve it further. With this model five mode shapes in the frequency range 100 - 3000 Hz are plotted in figures 8 to 11. As similar to the number two, mode shape three is again in the appendix. A sixth mode shape corresponding to 2524 Hz of frequency was predicted by the model. This frequency is visible in the experimental data, but as it is neglected in the analysis the mode shape is not represented nor considered in table 6.

The mode shapes are similar to the model with only one disk, and the considerations are also similar. Again the disks constitute a node in the vibration, and the amplitude is moved towards the extreme. The three systems obtained so far in this document will be referred to as *system I* for the only shaft configuration, *system II* shaft plus 100 mm disk, and *system III* shaft plus both disks.

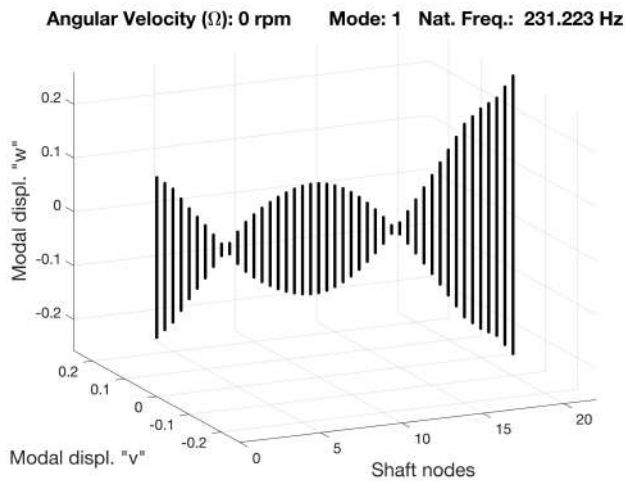


Figure 8: Mode shape 1, Shaft + 2 disks

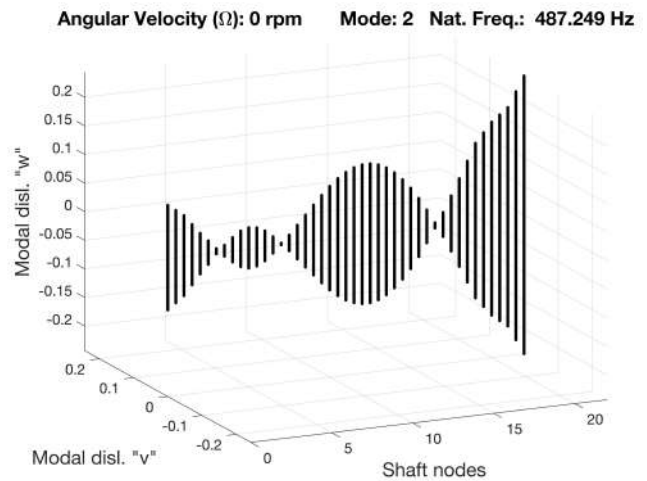


Figure 9: Mode shape 2, Shaft + 2 disks

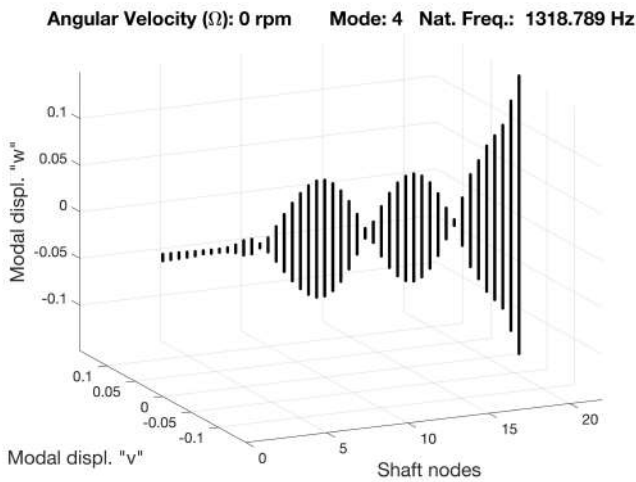


Figure 10: Mode shape 4, Shaft + 2 disks

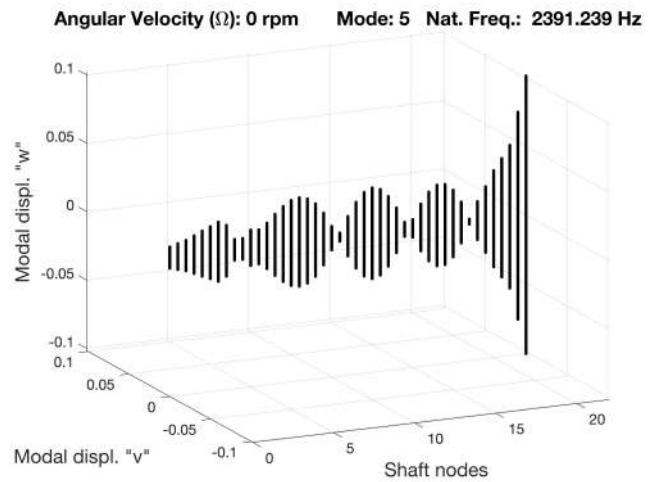


Figure 11: Mode shape 5, Shaft + 2 disks

3 Modelling the Ball Bearing and Coupling

In this chapter the three studied systems will be mounted on ball bearings, located in the designated spots of the shaft. In the FEM model bearings are represented by springs and dampers, therefore one wants to fill equation 3.16, where D is the dumping matrix associated with the bearing, K_B the stiffness matrix and q and F of course degrees of freedom and generalized forces respectively.

$$-D \cdot \dot{q} - K_B \cdot q = F \quad (3.16)$$

Ball bearings are characterized by high stiffness and low damping, therefore D is still neglected, $D \sim 0$. They are mounted in correspondence of shaft nodes, allowing for a simpler K_B matrix considering only stiffness in v and w direction, as in equation 3.17. All cross coupling effects, K_{vw} and K_{wv} , are zero in this case, and will be introduced in chapter 4 for hydrodynamic bearings.

$$K_B = \begin{bmatrix} K_{vv} & K_{vw} \\ K_{wv} & K_{ww} \end{bmatrix} = \begin{bmatrix} K_{vv} & 0 \\ 0 & K_{ww} \end{bmatrix} \quad (3.17)$$

This stiffness changes with the rotation speed, oscillating between a minimum and a maximum, but this effect is neglected throughout this analysis. In this stage of the study the speed Ω is still zero, ball bearing stiffness is considered symmetric ($K_{vv}=K_{vv}=K$) and equal for the two bearings throughout all the study in this chapter.

3.1 Bearing stiffness influence study

For system I a study is conducted considering the first eighth natural frequencies, including the low range ones, and zero velocity $\Omega = 0$. To study the stiffness influence in natural frequencies and mode shapes, K is run from a free free condition, $K = 10^1$ N/m, to simply supported, $K = 10^9$ N/m. The results of this study are visible in figure 12, where the frequencies correspond to only the X-Z plane mode shapes. These mode shapes are illustrated in figures 13 and 14, with dark colors for higher stiffness (in order yellow $K = 10$ N/m, orange $K = 10^8$ N/m and brown $K = 10^9$ N/m). First and last mode shape are used as illustrative examples, while the whole lot is moved appendix B (5). The stiffness were chosen based on graph 12, to highlight the K effects in the mode shapes.

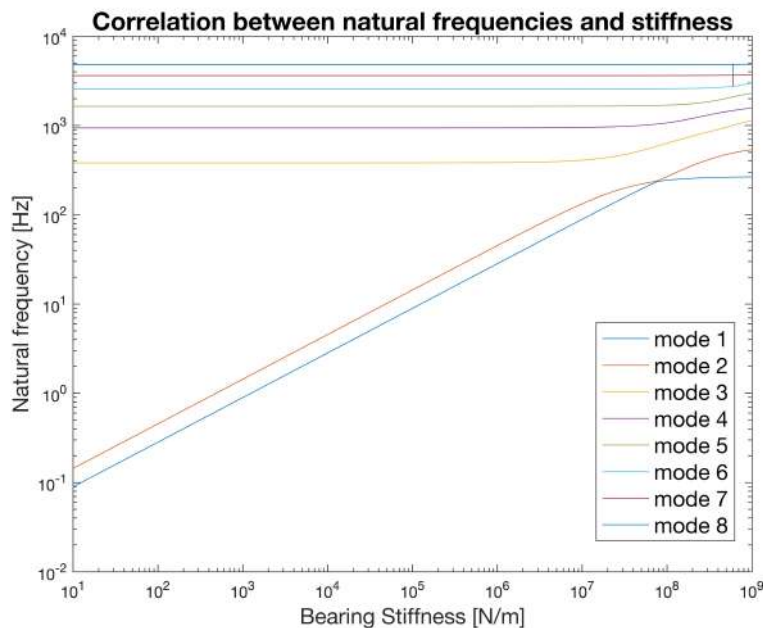


Figure 12: Shaft model - bearing stiffness influence on natural frequencies, $\Omega=0$

In the graph it is evident that the shaft model crosses three stages in the chosen range. In the first stage the stiffness K has great (\sim linear) influence in the natural frequencies, especially for the first two in the low range. Indeed here the frequency only depends on K , and the shaft only has rigid body motion. This can be confirmed looking at the first mode shape, figure 13, where for $K = 10$ N/m the shaft movement is completely rigid. The third phase corresponds to deflection of the shaft, where K has low influence, as illustrated by the plateau. The bearings are at this point

much more rigid than the shaft, which is forced to bend around them to copy with the vibration. This is again evident for $K = 10^8$ N/m and $K = 10^9$ N/m in figure 13, where the straight yellow line bends following the bearing constrain. Between these two phases deflections and rigid body motions are mixed, here the line is curved at approximately $K \sim 10^7$ - 10^8 N/m in figure 12.

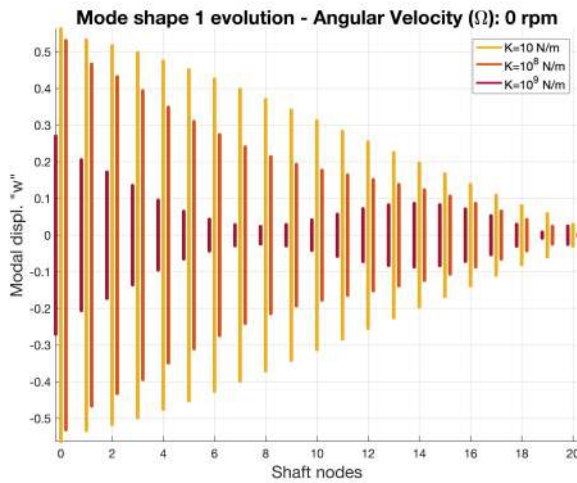


Figure 13: Combined mode shape 1

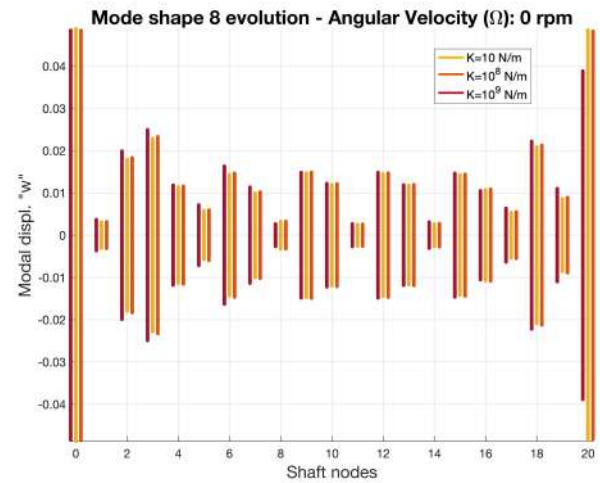


Figure 14: Combined mode shape 8

In figures 13 to 14 it is evident how in each mode shape increasing the stiffness reduces the amplitudes, creating new nodes in correspondence of the bearings, nodes 8 and 20. Darker color of the lines means higher stiffness. This is easy to see especially in the low frequency mode shapes, where the amplitude is greater. For the 8th mode shape for instance K has almost no influence, as evident in plot 12 as well.

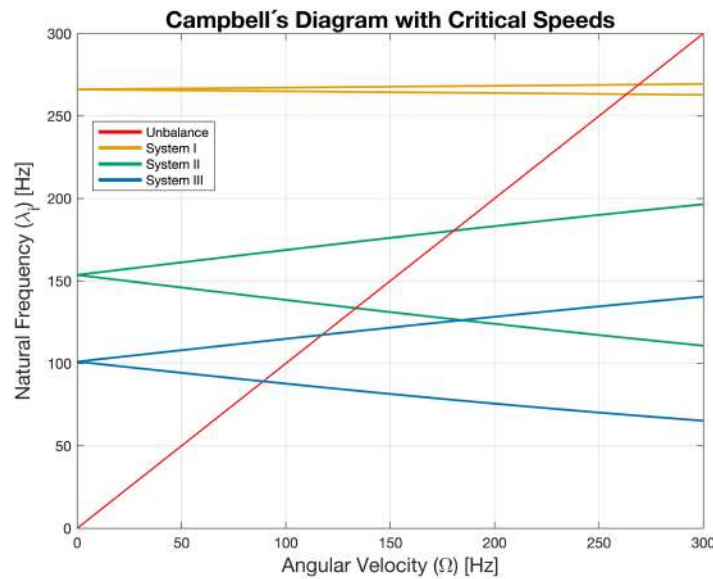
3.2 Prediction of Critical Speeds Using Two Ball Bearings

The analysis conducted so far was considering null rotating speed Ω . As this is by definition not the case in rotating machines, it is important to study the evolution of natural frequencies and resonances with speed. This is done using the Campbell diagram, which relates natural frequencies, i.e. Imaginary part of the eigenvalues, to rotating speed. Indeed, if so far in the analysis eigenvalues and eigenvectors were constant, they now are a function of Ω , as from 3.19 Matlab function. The general equation of the system, which still is a combination of the equations from the different FEM components, will now account for speed and gyroscopic effect, becoming equation 3.18, where damping D is negligible for ball bearings. Eigenvalues and eigenvector are calculated again with the process described in section 1.1.

$$M \cdot \ddot{q} + (-\Omega \cdot G + D) \cdot \dot{q} + K \cdot q = F \quad (3.18)$$

$$[U(\Omega), \lambda(\Omega)] = eig(-B, A(\Omega)) \quad (3.19)$$

With the ball bearings ($K = 10^9$ N/m) mounted in the three systems it is possible to create the diagram in figure 15. Here a very small amount of damping ($D \sim 0$) is added to avoid mathematical artefacts in the graph.

Figure 15: Campbell diagram for the three systems, $K = 10^9 \text{ N/m}$

In this Campbell's diagram, systems I to III are respectively yellow, green and blue, and the 45° inclined red line describes the speed path of the rotor. Each line represents a mode shape and a natural frequency for the system, respectively the upper line is the forward (*f.w.*) mode shape and bottom line the backwards (*b.w.*). This means that the rotor will have a secondary rotation in the same direction as Ω for forward mode, and in opposite direction for backward mode. As the rotor is symmetric ($K_{vv} = K_{ww} = K$) these mode shapes coincide for $\Omega = 0$, leading to symmetric movements in v and w as seen previously. For null velocity the natural frequencies are 266, 154 and 101 Hz. The first is visible in plot 12 for system I with the ultimate stiffness and the frequency-decreasing trend of the systems is the same discusses in pictures 13 to 14.

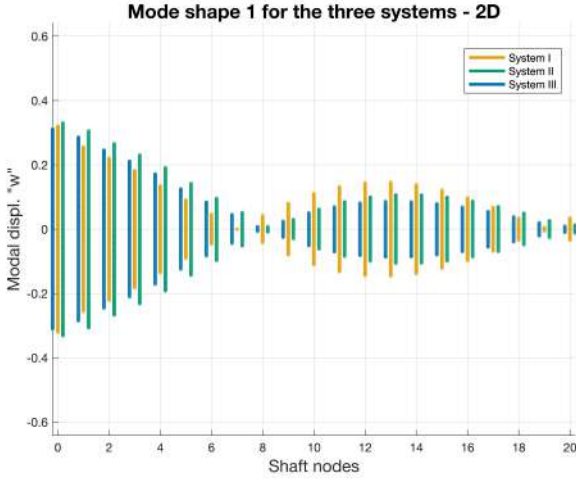
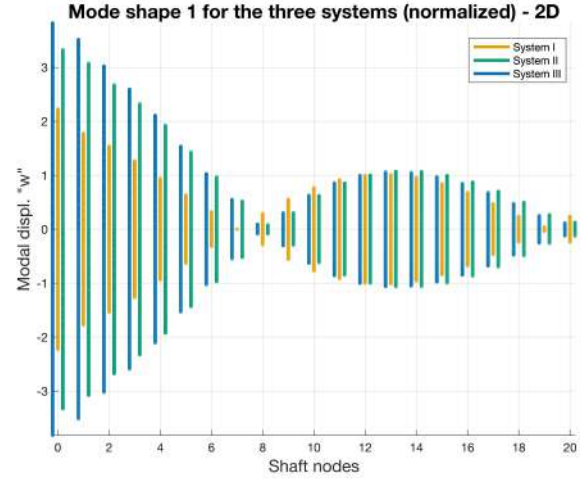
The natural frequencies λ_I vary as $f(\Omega)$. This is due to the gyroscopic effect, only activated when $\Omega \neq 0$ and the shaft bends, as evident in 3.18. System I (yellow) has little variation between *f.w.* and *b.w.* modes, as here the G effect is only given by the shaft. For systems II and III (green and blue) G effect is much higher due to the presence of the disks, leading to greater separation of *f.w.* and *b.w.* modes. Systems II and III look similar in terms of gyroscopic effect, but their difference is more easily visible in other mode shapes than the first, as illustrated in the plot from appendix C (5). This can be due to the type of movement of each mode, which bends more or less the shaft, other than the speed.

	System I	System II	System III
<i>f.w.</i> critical speed Ω_c [Hz]	269.1	180.4	117.2
<i>b.w.</i> critical speed Ω_c [Hz]	263.2	133.5	89.1

Table 7: Critical speeds for systems I to III

Table 7 reports the critical speeds, i.e. the speeds causing resonance, for the system. The meeting point of the red line with the systems' ones on the Campbell diagram determines these speeds. The mode shapes become 3D for $\Omega \neq 0$ and form circular trajectories due to the system's symmetry. Figure 16 shows an overlap of the first mode shapes for the three systems using the same

colors as in figure 15. The disks increase the oscillation amplitude, but it seems to have little effect on the shaft movements. Figure 17 normalizes the amplitudes with respect to the 13th node values, highlighting the disks' influence in the mode shape. The oscillation of the disks is evident compared to the shaft-only model. A set of 3D plots in appendix B (5) further illustrates this phenomenon.

Figure 16: 1st mode shape - 2DFigure 17: 1st normalized mode shape - 2D

3.3 Unbalance Response Using Two Ball Bearings

To prevent catastrophic failure, the maximum vibration amplitude at the disk locations in a supercritical rotating compressor must not exceed $30 \mu m$, which requires studying the maximum unbalance in the 100 mm disk of system III. The 80 mm disk and shaft are assumed to be perfectly balanced, while the bearing stiffness is the final $K = 10^9$ N/m symmetric and equivalent in the two bearings.

The presence of an unbalanced mass in the system causes a force that can be decomposed in the v and w direction, y and z axis. Using Euler formulation these forces can be re-arranged as in equation 3.20, dividing them in forward and backward force. In the FEM model these forces will be placed in the unbalance node, completing the linear system 3.18. Assuming the solutions of the system as $\bar{X}_f(t) = \bar{X}_f \cdot e^{i\Omega t}$ and $\bar{X}_b(t) = \bar{X}_b \cdot e^{-i\Omega t}$ one can solve the system and get the general permanent solution as in 3.21. This permanent solution \bar{X}_p corresponds to the amplitude of the vibration, which needs to be below $30 \mu m$ in this study.

$$f_f(t) = f_f \cdot e^{i\Omega t} \quad f_b(t) = f_b \cdot e^{-i\Omega t} \quad (3.20)$$

$$\bar{X}_p = \bar{X}_f + \text{conj}(\bar{X}_b) \quad (3.21)$$

Due to symmetry of the system the presence of the unbalance will cause resonance only for the $f.w.$ mode shape, therefore the study is limited to the upper line in Campbell's diagram. If the excitation was due to external forces instead, also the $b.w.$ mode would be activated once the force frequency matches the critical frequency of the system. Symmetry involves that the mode shape

is simply circular, as in figures 16 and 17, and not elliptical (combination of $f.w.$ and $b.w.$) as it would be for asymmetric systems, as happens for hydrodynamic bearings.

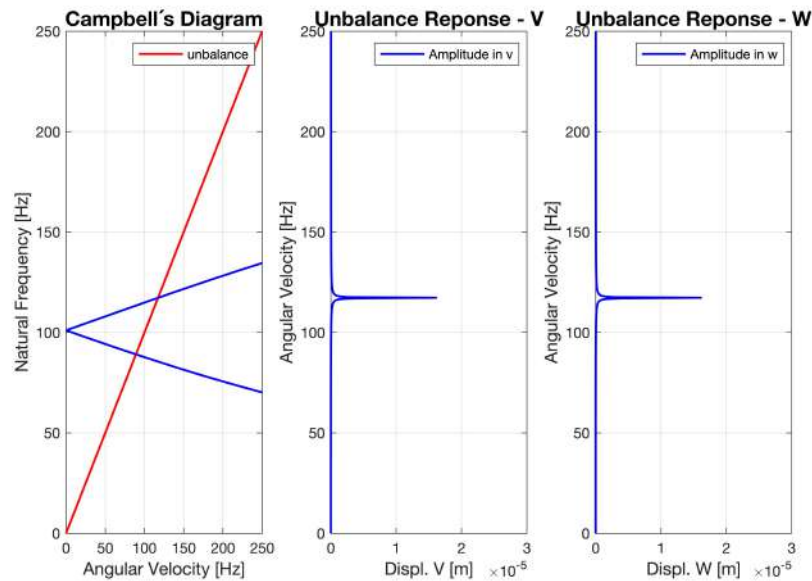


Figure 18: Study of the first resonance in system III

In figure 18 a mass on $1g$ is used at a distance of $1mm$ in the $100mm$ disk node. When crossing the critical speed an amplifications is visible in the right graphs, in the Frequency Response Function (FRF) of the signal. The peak describes the movement amplitude of the shaft in the two directions, reaching values of $\sim 16\mu m < 30\mu m$ for this unbalance. In such a big rotor, a unbalance of only $1g \cdot mm$ is of course not realistic, so the design specification are not met. Such a drastic amplitude is due to the complete absence of damping in the model, indeed not only the bearings are considered as perfectly stiff, but also the shaft and its housing is considered to have no damping. This is further confirmed by the model, as if the discretization of right graphs is increased, the peak becomes even sharper, leading to the amplitude theoretically go toward infinite.

4 Modelling the Hydrodynamic Bearing and Coupling

In the next chapter, a journal bearing is modeled using springs and dampers as described in chapter 3. Hydrodynamic bearings are more complex to model due to their non-linear stiffness, damping, and cross-coupling effects. These bearings consist of a bushing that maintains a constant flow of oil to prevent overheating and friction. During rotation, the shaft moves the oil, creating a lubricant layer that separates it from the bushing.

Assumptions for the model include laminar oil flow between the shaft and bushing, neglect of oil inertia and temperature changes, and consideration of oil as a non-compressible Newtonian fluid with constant pressure. While these assumptions simplify the model, it's important to note their limitations, particularly at higher speeds where turbulence may occur.

To model the bearing one needs to find the forces given by the oil layer. Taking a portion of fluid it is possible to find the velocity from the equilibrium of shear forces and pressure. Knowing that due to the non slip condition the fluid speed corresponds to Ω close to the shaft and is null

close to bushing, it is possible to integrate along the area to find the flow Q . This Q is constant due to incompressibility, so setting the derivative as zero and with some adjustments one finds the Reynolds Equation for bearings with finite dimensions, equation 4.22.

$$\frac{\partial}{\partial x} \left(h^3 \frac{\partial p}{\partial x} \right) + \frac{\partial}{\partial z} \left(h^3 \frac{\partial p}{\partial z} \right) = 6\eta U \frac{\partial h}{\partial x} + 12\eta \frac{\partial h}{\partial t} \quad (4.22)$$

Here the oil film thickness is indicated with h , η is the dynamic viscosity, p is the oil film pressure, U the linear velocity at the shaft interface, x and z circumferential and longitudinal directions. The last term in the equation is the squeeze effect, due to the oscillations of the shaft that compresses and expands the oil. From the equation it is evident how without gradient $\partial h / \partial x$ there are no forces $\partial p / \partial x$ and $\partial p / \partial z$ acting on the shaft. This highlights the fact that when the rotor is perfectly centred in the bushing there are no hydrodynamics forces acting (F_H), so eccentricity is fundamental to have forces F_x and F_y .

This is a fundamental point for hydrodynamic bearings, as the gradient is fundamental for their correct operation. With equation 4.22 pressure is defined as a function of geometrical parameters and time, $p = f(x, z, t)$, and one can integrate this along the area to find the actual forces on the shaft (see appendix A (5), equation 5.40).

In equation 5.40 the non linear forces are then a function of position and velocity. These can be linearized using Taylor expansion, getting the system in matrix form, from which it is possible to extract stiffness and damping matrices K and D , equation 4.23. Here the rotor movements are described with Δ . These F_H forces and the related K and D matrices are given in the equilibrium position, where the shaft weight matches the oil pressure.

$$F_H = \begin{Bmatrix} F_{Hx} \\ F_{Hy} \end{Bmatrix} = \begin{bmatrix} K_{xx} & K_{xy} \\ K_{yx} & K_{yy} \end{bmatrix} \begin{Bmatrix} \Delta_{Xr} \\ \Delta_{Yr} \end{Bmatrix} + \begin{bmatrix} D_{xx} & D_{xy} \\ D_{yx} & D_{yy} \end{bmatrix} \begin{Bmatrix} \dot{\Delta}_{Xr} \\ \dot{\Delta}_{Yr} \end{Bmatrix} \quad (4.23)$$

4.1 Static and Dynamic Properties

The Journal Bearing Databook [1] is used to find bearing parameters such as stiffness and damping ratio. Parameters for journal bearings include clearance, preload factor, and L/d ratio. The study focuses on system II: here a two-axial groove bearing, L/D ratio of 0.5 is used in the left position. The right bearing is the same ball bearing with $K = 10^9$ N/m used before. The study evaluates operational range, stability margin, and maximum vibration amplitude due to unbalance.

The procedure to identify bearing parameters involves calculating the Sommerfeld number using equation 4.24 and finding the appropriate $K_{i,j}$ and $D_{i,j}$ from the tables in Appendix E (5). The S number is based on speed Ω and factors in geometrical and operational parameters such as L , d , C_p , R , viscosity μ , weight W , and velocity N (Hz). The static load W can be found from equilibrium of the shaft. This is done in Appendix D (5), resulting in $W_1 = 892.7$ N and $W_2 = 45.0$ N for the two bearings.

$$S = \frac{\mu N L d}{W} \left(\frac{R}{C_p} \right)^2 \quad (4.24)$$

As S depends on the velocity, also the stiffness and damping of the bearing ($K_{i,j}$ and $D_{i,j}$) will be a function of Ω . So if in ball bearings only the gyroscopic effect G was function of speed

($G(\Omega)$) now also $K(\Omega)$ and $D(\Omega)$ are. The known equation to characterize the system then becomes equation 4.25.

$$M \cdot \ddot{q}(t) + (D(\Omega) + G(\Omega))\dot{q}(t) + K(\Omega)q(t) = F(t) \quad (4.25)$$

In what follows capital D and L will indicate diameter and length of the bearing, and small d and l the equivalent for the shaft. For the specific type of oil the viscosity is $\eta = 0.0277 \cdot e^{0.034 \cdot (40-55)}$, where 55 is the temperature, considered constant. Having a clearance of $100 \mu m$ and a shaft ratio r of $99.6/2 \text{ mm}$ it is possible to find the bearing ratio R from $C=R-r$ and the diameter D accordingly. L is then found from L/D which is 0.5 for the given bearing.

As anticipated, during rotation the shaft moves oil towards the bottom, changing its position (eccentricity) in the bearing and modifying its gradient. Using the journal bearing data from the tables one can illustrate the oil film thickness evolution with speed Ω , figure 19. As S number is proportional to speed N similar considerations can be done plotting S in the x axis. The oil film thickness is calculated from $h = D/2 - d/2 - \sqrt{x_{st}^2 + y_{st}^2}$, where the x_{st} and y_{st} coordinates are given indirectly from the tables, using eccentricity and attitude angle.

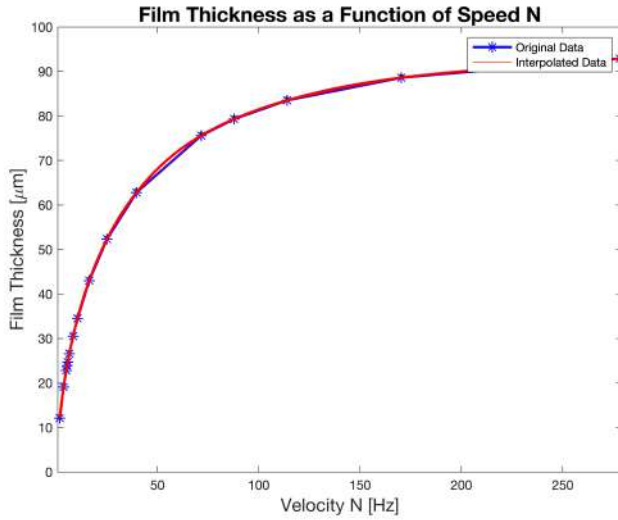


Figure 19: Film thickness evolution with speed

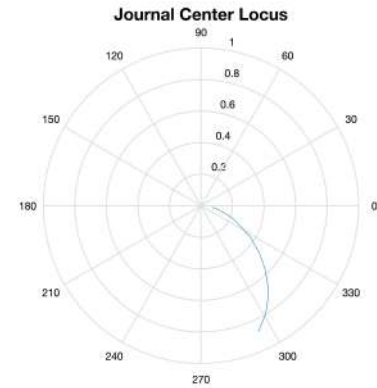


Figure 20: Locus evolution

Figure 19 summarized the overall behaviour: increasing Ω the eccentricity goes towards 0 and the attitude angle goes towards 90° . This translates in a lift up of the shaft which will progressively move towards the center, where the oil film is $100 \mu m$, as evident in figure 20. As evident from equation 4.22 this thickness reduction cuts the forces on the shaft, causing instability.

Here and in the following plots the Matlab function *interp1* is used to interpolate the data, to get a better definition of the coefficients. Original data is left in blue and linearly interpolated, while in red a *spline* interpolation is given. The same spline interpolation is used to extract the table data with more precision.

Taking dimensionless stiffness and damping coefficients from the table in appendix C, it is possible to calculate k_{ij} and d_{ij} as $k_{ij} = W/C \cdot K_{ij}$ and $d_{ij} = W/(C\omega) \cdot B_{ij}$. These can be plotted again against velocity, with blue being original data and red interpolated one, plots 21 and 22.

It is here evident how increasing N and with the shaft moving towards the center the bearing dangerously loses damping capacity, approaching instability. This is also evident from the formula-

tion of $d_{i,j}$, with ω in the denominator. This effect is due to the movement of oil, which thanks to the shaft rotation is unable to move to the sides, absorbing energy from the vibrations, and remains stuck impeding damping effect and increasing the stiffness.

The cross coupling effects are responsible for moving the energy from one direction to the other, deviating the movements from the two main axis. In journal bearings the K matrix is not symmetric and the signs of the elements determine the operating conditions. In stable load conditions k_{xy} and k_{yx} have different values but same sign. The plots show that as the speed increases and the shaft approaches instability, k_{xy} and k_{yx} become increasingly different in magnitude and sign. When the shaft is centered, k_{xx} equals k_{yy} and k_{xy} has opposite sign than k_{yx} . The oil distribution around the shaft is symmetric at that point, as from figure 20 representing the locus.

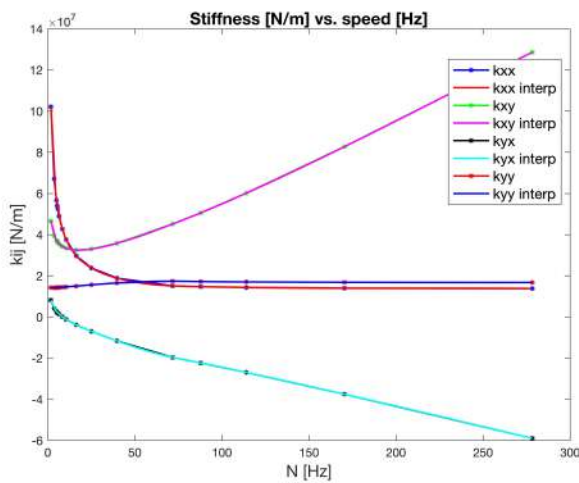


Figure 21: Stiffness evolution with speed

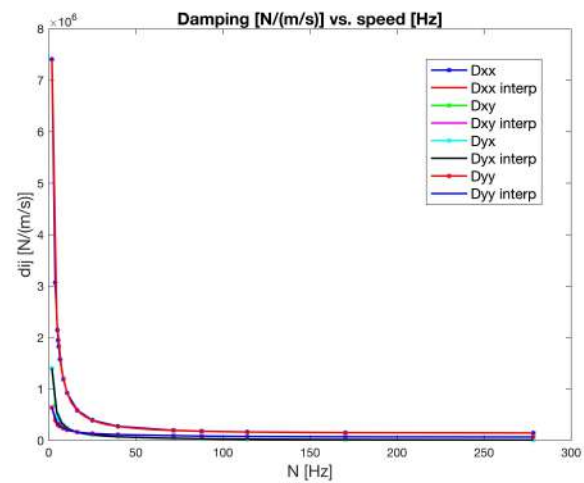


Figure 22: Damping evolution with speed

4.2 Prediction of critical speeds and stability limit

Once added to system II the journal bearing, using all $k_{i,j}$ and $d_{i,j}$ terms and keeping $k = 10^9$ N/m for the ball bearing, it is possible to predict the critical speeds of the system. As anticipated in chapter 3 the compressor is a supercritical rotating machine, set to operate between the first two critical speeds. These can be found from the Campbell's diagram, figure 23, looking at where the unbalance line meets the system's natural frequencies. The process is the same described in section 3.2, as evident the lines meet at $N \simeq 140.2$ Hz and $N \simeq 248.6$ Hz, corresponding to $\simeq 8400$ rpm and $\simeq 14900$ rpm.

By simple subtraction the operational range with these bearings is limited to only 6500 rpm in size, with potential vibration and rubbing issues if operated above 14900 rpm, resulting in possible failure. However, the 14900 rpm speed limit is reasonable as such large machines generally operate at lower speeds.

In figure 23 the first natural frequency to be crossed is the one corresponding to the second backwards mode shape, and the second is the second forward. This Campbell's diagram is different from the one in figure 15 for only ball bearings, mainly due to the presence of damping. One of the effect of damping is evident in the bottom natural frequency, which lays flat on $\lambda_I = 0$ (damping factor will be 1) up to roughly the second critical speed, where the associated movement passes from

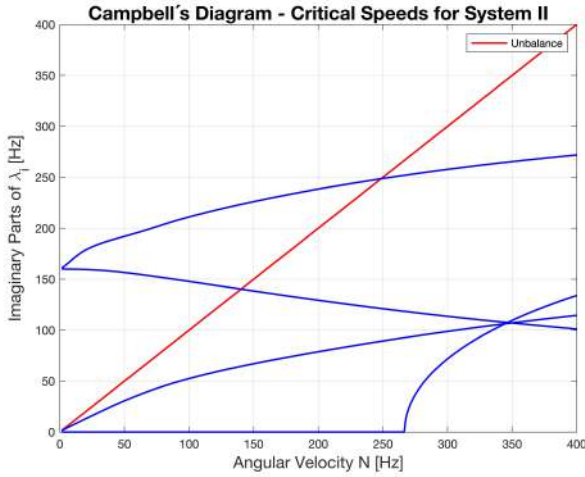


Figure 23: Campbell diagram - system II

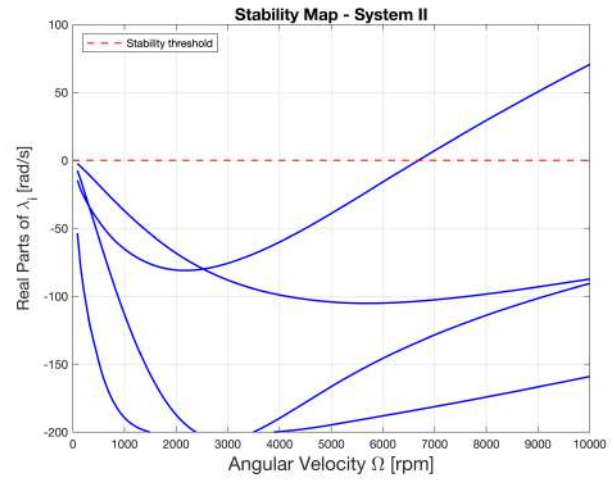


Figure 24: Stability map - system II

overdamped to underdamped, and the natural frequency suddenly rises. This is the same change of damping described in figure 22, and discussed in section 4.1.

The eigenvalues and eigenvectors of the system, calculated as in chapter 3, yield a function $\lambda(\Omega)$ which depends on the speed. Compared to a system with only ball bearings, the system is more complex due to non-zero damping and λ_R . The relationship of all parameters with rotational speed is critical in defining the stability zone, where the machine can operate safely.

The sign of $\lambda_R(\Omega)$ determines instability and can be plotted in a stability diagram against speed Ω , as shown in figure 24. This diagram represents the trend of the real part of each natural frequency over speed. Instability arises from the transient solution, while unbalance is linked to the permanent solution. An unstable operating condition is defined as $\lambda_R(\Omega) > 0$, where vibrations persist once triggered. When approaching the stability limit of a rotating machine, the transient solution dominates over the permanent one, making unbalance effects negligible compared to instability effects.

By looking at the stability map in figure 24 instability is first reached at $\Omega \simeq 6686$ rpm, or 111.4 Hz, therefore $N_{max} = 6686$ rpm. This is the maximum speed for the system to avoid instability due to the oil - shaft interaction, and the reduction of damping and oil forces.

It is soon evident that the instability limit is lower than the first critical speed. The machine cannot operate over or close to the instability limit, therefore the effective operational range is only up to roughly 6600 rpm. This means that the compressor does not meet the requirements, and major changes are needed for it to operate between the critical speeds.

Nevertheless, one can find the natural frequency corresponding to this instability threshold. As at N_{max} $\lambda_R = 0$ it is sufficient to identify the associated imaginary part λ_I : this is the frequency of unstable vibration, not the rotating speed of the shaft. From the Matlab code its easy to spot where λ_R changes sign, and taking the imaginary part yields to $\lambda_I = 56$ Hz. Calculating the ratio between this unstable frequency and the rotor angular velocity N_{max} in Hz yields to:

$$\frac{\lambda_I[\text{Hz}]}{N_{max}[\text{Hz}]} = \frac{56}{109.2} = 0.51$$

So the vibration frequency of the system is not the same frequency as the rotation, but roughly half. This ratio of $\simeq 0.5$ is observed to be a constant in these types of rotating machines, and confirms that the results and the plots are accurate.

4.3 Unbalance response

One can at this point calculate the maximum tolerable unbalance to avoid rubbing in the compressor. The shaft and 80 mm disks are again assumed to be balanced, with unbalance only in the 100 mm disk, and the maximum vibration amplitude at the disk locations is $30\mu\text{m}$. The stiffness of the ball bearing is kept $K = 10^9 \text{ N/m}$. The procedure is in all similar to what done in section 3.3, calculating the forward and backwards forces as in equation 3.20 and finding the permanent solutions with equation 3.21. Done this it is possible to plot, next to Campbell's diagram, the FRF of the maximum amplitude, in figure 25. Due to asymmetry of the stiffness the orbit is now elliptical, and the two displacements need to be summed under squared root to find the maximum circle that circumscribes the ellipsis.

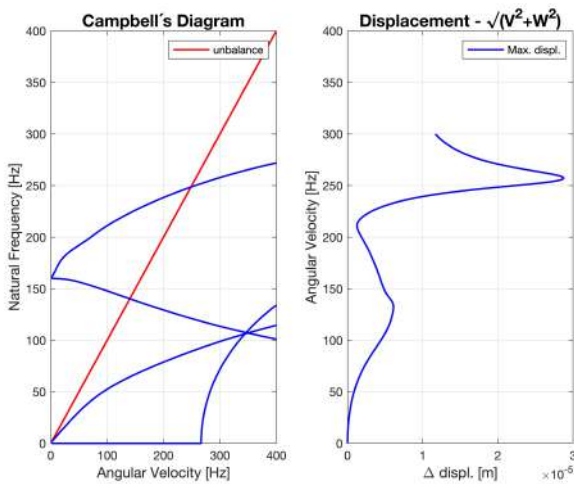


Figure 25: Unbalance response of system II

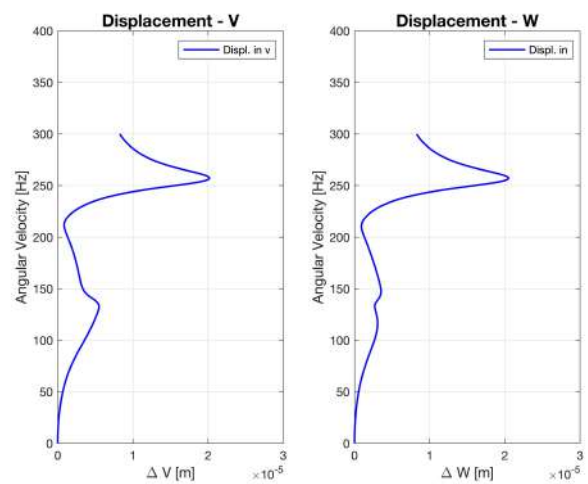


Figure 26: Displacements in V and W

The maximum possible unbalance is found to be $\simeq 200 \text{ g}\cdot\text{mm}$, much better than the one found for ball bearings, as they were not damped. This is the one plotted in figure 25, with the Campbell's diagram being the same as in figure 23. In figure 26 the displacements V and W are illustrated to highlight the orbit asymmetry.

A $200 \text{ g}\cdot\text{mm}$ unbalance seems reasonable, and looking at the related displacements the system would be safe to operate across the first critical speed and up to over the second with this unbalance. The wavy shape of the V and W displacement can be associated with the presence of damping. The peaks corresponding to the system crossing the critical speeds are not as sharp as they were in figure 18 for the ball bearing system. Overall the vibrations levels are much smaller thanks to the lower stiffness and especially higher damping offered by the hydrodynamic bearing, making it in general a better choice for these specific application compared to ball bearings. Nevertheless, with an instability limit of $\simeq 6600 \text{ rpm}$ the compressor is not usable in the desired range with these bearings.

4.4 Engineering Design

Finally, also the second bearing will be substituted by a hydrodynamic bearing, to compare the three configurations. This second bearing will have the same characteristics of the first, so $L/D=0.5$, but a diameter of $d = 50$ mm of the shaft in that point and a clearance of $85\mu\text{m}$.

The procedure used to extrapolate the bearing data is the same, using the spline interpolation to get a better approximation. The Sommerfeld number is calculated for each speed and used for the interpolation. Static forces $W_2=45\text{N}$ and $W_1=892.7\text{N}$ were previously calculated.

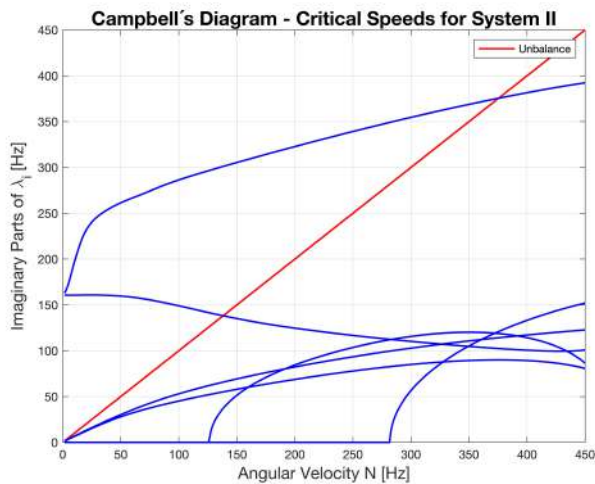


Figure 27: Campbell diagram - HD bearings

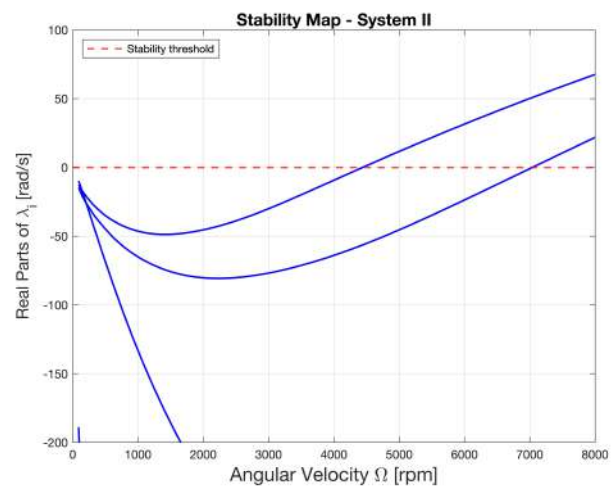


Figure 28: Stability map - HD bearings

The new Campbell's diagram and stability diagram for this full hydrodynamic bearing (HD) configuration are in figure 27 and 28. In this configuration instability is first reached at 4440 rpm, or 74 Hz. The first critical speed is 138.1 Hz or $\simeq 8280$ rpm and second is 375.5 in Hz $\simeq 22530$ rpm.

Using both hydrodynamic bearings leads to a much larger operational range, with the first two critical speeds separated by 14250 rpm compared to the 6500 rpm of the previous configuration. This is due to the different stiffness and damping conditions offered by the second bearing, which results in a bigger opening of the two natural frequencies lines in Campbell's diagram. However, the difference between using one or two hydrodynamic bearings is not as significant as the difference between a full ball bearing configuration and one hydrodynamic bearing, because the second bearing has less influence on the system dynamics than the first, due to the limited weight on it.

The stability margin on the other hand is even worse in this configuration, with the first λ_R becoming positive already at 4440 rpm, and making the machine unusable at higher speeds. This is also due to the low weight on the second bearing, which allows the shaft to rapidly move towards the center, losing eccentricity and damping capacity.

Overall the second hydrodynamic bearing induces more instability in the system, making the compressor unstable already at $\simeq 4400$ rpm. As a further step in the design, one could consider modifying the bearing clearance or changing type of bearings with active systems, that can change the damping and move the instability limit to higher speeds. Otherwise, the operation range of the compressor is limited to 4400 rpm, which is probably not satisfactory for this machine.

List of Figures

1	Shaft element with degrees of freedom	1
2	Mode shape 1 - Shaft only	5
3	Mode shape 4 - Shaft only	5
4	Mode shape 1, Shaft + 1 disk	7
5	Mode shape 2, Shaft + 1 disk	7
6	Mode shape 4, Shaft + 1 disk	7
7	Mode shape 5, Shaft + 1 disk	7
8	Mode shape 1, Shaft + 2 disks	9
9	Mode shape 2, Shaft + 2 disks	9
10	Mode shape 4, Shaft + 2 disks	9
11	Mode shape 5, Shaft + 2 disks	9
12	Shaft model - bearing stiffness influence on natural frequencies, $\Omega=0$	10
13	Combined mode shape 1	11
14	Combined mode shape 8	11
15	Campbell diagram for the three systems, $K = 10^9 N/m$	12
16	1 st mode shape - 2D	13
17	1 st normalized mode shape - 2D	13
18	Study of the first resonance in system III	14
19	Film thickness evolution with speed	16
20	Locus evolution	16
21	Stiffness evolution with speed	17
22	Damping evolution with speed	17
23	Campbell diagram - system II	18
24	Stability map - system II	18
25	Unbalance response of system II	19
26	Displacements in V and W	19
27	Campbell diagram - HD bearings	20
28	Stability map - HD bearings	20
29	Mode shape 2 - Shaft only	V
30	Mode shape 3 - Shaft only	V
31	Mode shape 3, Shaft + 1 disk	VI
32	Mode shape 3, Shaft + 2 disks	VI
33	Combined mode shape 1	VI
34	Combined mode shape 2	VI
35	Combined mode shape 3	VII
36	Combined mode shape 4	VII
37	Combined mode shape 5	VII
38	Combined mode shape 6	VII
39	Combined mode shape 7	VIII
40	Combined mode shape 8	VIII
41	1 st mode shape - 3D	VIII
42	1 st mode shape - 2D	VIII
43	1 st normalized mode shape - 3D	IX
44	1 st normalized mode shape - 2D	IX

45	Stiffness evolution with speed	IX
46	Damping evolution with speed	X
47	Campbell diagram extended	XI
48	Static equilibrium of the shaft with diagrams	XII

List of Tables

1	Convergence study with five levels of discretization	3
2	Discrepancy between experimental natural frequencies and model - shaft only	4
3	Final model of the shaft with dimensions, <i>initial shaft model</i>	4
4	Comparison between theoretical model and experiments	4
5	One disk - results from all models and discrepancies	6
6	Two disks - results from all models and discrepancies	8
7	Critical speeds for systems I to III	12
8	Bearing data for Two-axial-groove, $L/D = 0.5$ journal bearing	XIII

References

- [1] T. Someya, *Journal-Bearing Databook*. Springer, 1989th ed., August 2014.

5 Appendix

Appendix A - Supplementary equations

Full collection of shape functions from section 1.1 in equations from 5.26 to 5.29. Here l is the length of the element.

$$\psi_1(x') = 1 - \frac{3}{l^2}x'^2 + \frac{2}{l^3}x'^3 \quad \theta_1(x') = \dot{\psi}_1(x') = -\frac{6}{l^2}x' + \frac{6}{l^3}x'^2 \quad (5.26)$$

$$\psi_2(x') = x' - \frac{2}{l}x'^2 + \frac{1}{l^2}x'^3 \quad \theta_2(x') = \dot{\psi}_2(x') = 1 - \frac{4}{l}x' + \frac{3}{l^2}x'^2 \quad (5.27)$$

$$\psi_3(x') = 3\frac{x'^2}{l^2} - 2\frac{x'^3}{l^3} \quad \theta_3(x') = \dot{\psi}_3(x') = \frac{6}{l^2}x' - \frac{6}{l^3}x'^2 \quad (5.28)$$

$$\psi_4(x') = -\frac{x'^2}{l} + \frac{x'^3}{l^2} \quad \theta_4(x') = \dot{\psi}_4(x') = -\frac{2}{l}x' + \frac{3}{l^2}x'^2 \quad (5.29)$$

From section 1.1 all the mathematical passages to go from the shape functions to the matrices are in the following equations.

For each shaft element the degrees of freedom can be expressed as in equation 1.3 and the shape functions as in equations 5.30 and 5.31. In equations 5.32 and 5.33 the shape functions are multiplied by the degrees of freedom, giving translations and rotations of the element at a given coordinate x' and in time t , as q changes in time.

$$\Psi(x') = \begin{bmatrix} \psi_1(x') & 0 & 0 & \psi_2(x') & \psi_3(x') & 0 & 0 & \psi_4(x') \\ 0 & \psi_1(x') & -\psi_2(x') & 0 & 0 & \psi_3(x') & -\psi_4(x') & 0 \end{bmatrix} \quad (5.30)$$

$$\Theta(x') = \begin{bmatrix} \Theta_\beta(x') \\ \Theta_\Gamma(x') \end{bmatrix} = \begin{bmatrix} 0 & -\theta_1(x') & \theta_2(x') & 0 & 0 & -\theta_3(x') & \theta_4(x') & 0 \\ \theta_1(x') & 0 & 0 & \theta_2(x') & \theta_3(x') & 0 & 0 & \theta_4(x') \end{bmatrix} \quad (5.31)$$

$$\begin{Bmatrix} V(x', t) \\ W(x', t) \end{Bmatrix} = \Psi(x')q(t) \quad (5.32) \quad \begin{Bmatrix} \beta(x', t) \\ \Gamma(x', t) \end{Bmatrix} = \Theta(x')q(t) \quad (5.33)$$

The matrices obtained in section 1.1 are reported below. These are stiffness matrix K and mass matrices M_T and M_R due to rotations and translations respectively. G_S is the gyroscopic matrix of each shaft element.

$$K_B = \frac{EI}{l^3} \begin{bmatrix} 12 & & & & & & & \\ 0 & 12 & & & & & & \\ 0 & -6l & 4l^2 & & & & & \\ 6l & 0 & 0 & 4l^2 & & & & \\ -12 & 0 & 0 & -6l & 12 & & & \\ 0 & -12 & 6l & 0 & 0 & 12 & & \\ 0 & -6l & 2l^2 & 0 & 0 & 6l & 4l^2 & \\ 6l & 0 & 0 & 2l^2 & -6l & 0 & 0 & 4l^2 \end{bmatrix} \quad (5.34)$$

$$M_T = \frac{\mu l}{420} \begin{bmatrix} 156 & & & & & & & \\ 0 & 156 & & & & & & \\ 0 & -22l & 4l^2 & & & & & \\ 22l & 0 & 0 & 4l^2 & & & & \\ 54 & 0 & 0 & 13l & 156 & & & \\ 0 & 54 & -13l & 0 & 0 & 156 & & \\ 0 & 13l & -3l^2 & 0 & 0 & 22l & 4l^2 & \\ -13l & 0 & 0 & -3l^2 & -22l & 0 & 0 & 4l^2 \end{bmatrix} \quad (5.35)$$

$$M_R = \frac{\mu r^2}{120l} \begin{bmatrix} 36 & & & & & & & \\ 0 & 36 & & & & & & \\ 0 & -3l & 4l^2 & & & & & \\ 3l & 0 & 0 & 4l^2 & & & & \\ -36 & 0 & 0 & -3l & 36 & & & \\ 0 & -36 & 3l & 0 & 0 & 36 & & \\ 0 & -3l & -l^2 & 0 & 0 & 3l & 4l^2 & \\ 3l & 0 & 0 & -l^2 & -3l & 0 & 0 & 4l^2 \end{bmatrix} \quad (5.36)$$

$$G_S = \frac{2\mu r^2}{120l} \begin{bmatrix} 0 & & & & & & & \\ 36 & 0 & & & & & & \\ -3l & 0 & 0 & & & & & \\ 0 & -3l & 4l^2 & 0 & & & & \\ 0 & 36 & -3l & 0 & 0 & & & \\ -36 & 0 & 0 & -3l & 36 & 0 & & \\ -3l & 0 & 0 & l^2 & 3l & 0 & 0 & \\ 0 & -3l & -l^2 & 0 & 0 & 3l & 4l^2 & 0 \end{bmatrix} \quad (5.37)$$

Below the transformation matrices for each rotation are reported.

$$\mathbf{T}_\phi = \begin{bmatrix} 1 & 0 & 0 \\ 0 & \cos \phi & \sin \phi \\ 0 & -\sin \phi & \cos \phi \end{bmatrix}$$

$$\mathbf{T}_\Gamma = \begin{bmatrix} \cos \Gamma & \sin \Gamma & 0 \\ -\sin \Gamma & \cos \Gamma & 0 \\ 0 & 0 & 1 \end{bmatrix}$$

$$\mathbf{T}_\beta = \begin{bmatrix} \cos \beta & 0 & -\sin \beta \\ 0 & 1 & 0 \\ \sin \beta & 0 & \cos \beta \end{bmatrix}$$

Below mass and gyroscopic matrix for the disk element, from chapter 2.

$$M = \begin{bmatrix} m_D & 0 & 0 & 0 \\ 0 & m_D & 0 & 0 \\ 0 & 0 & I_D & 0 \\ 0 & 0 & 0 & I_D \end{bmatrix} \quad (5.38) \quad G_D = \begin{bmatrix} 0 & 0 & 0 & 0 \\ 0 & 0 & 0 & 0 \\ 0 & 0 & 0 & -I_P \\ 0 & 0 & I_P & 0 \end{bmatrix} \quad (5.39)$$

Integration of pressure along area in a hydrodynamics bearing to find the oil forces on the shaft.

$$F_H = \int_A p dA \Rightarrow \begin{cases} F_x \\ F_y \end{cases} = \begin{cases} F_x(x, \dot{x}, y, \dot{y}) \\ F_y(x, \dot{x}, y, \dot{y}) \end{cases} \quad (5.40)$$

Appendix B - Supplementary mode shape plots

Images 29 to 30 collect the second and third mode shape of the shaft only model, from section 1.3 of the document.

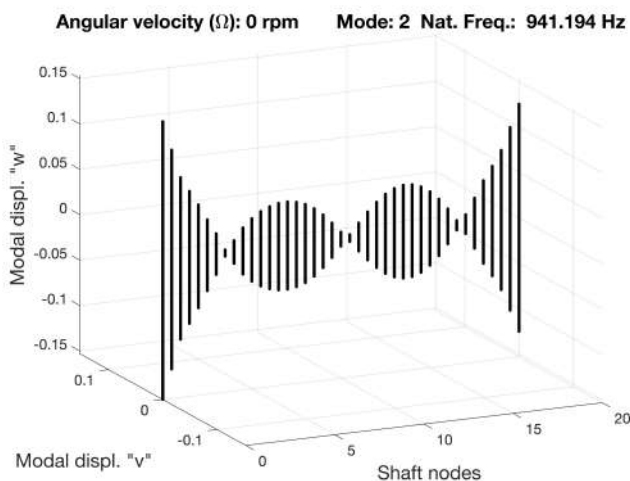


Figure 29: Mode shape 2 - Shaft only

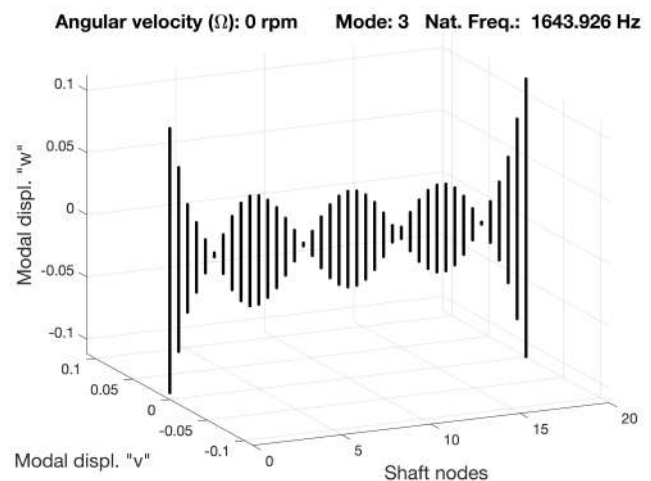


Figure 30: Mode shape 3 - Shaft only

Image 31 is the third mode shape for the shaft + one disk model. Image 32 is the third mode shape for the shaft + two disks model.

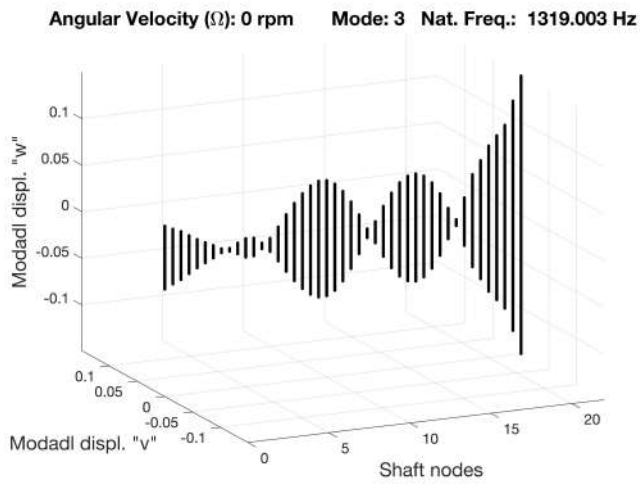


Figure 31: Mode shape 3, Shaft + 1 disk

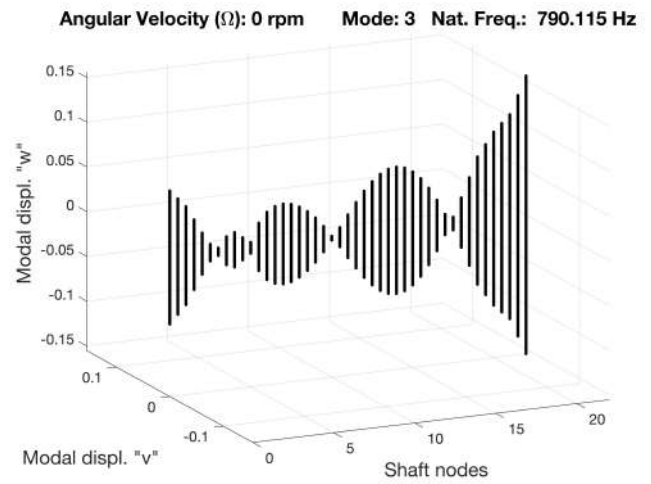


Figure 32: Mode shape 3, Shaft + 2 disks

Figures 33 to 33 illustrate the whole lot of mode shapes from section 3.1. These are described with different colors for increasing ball bearing stiffness.

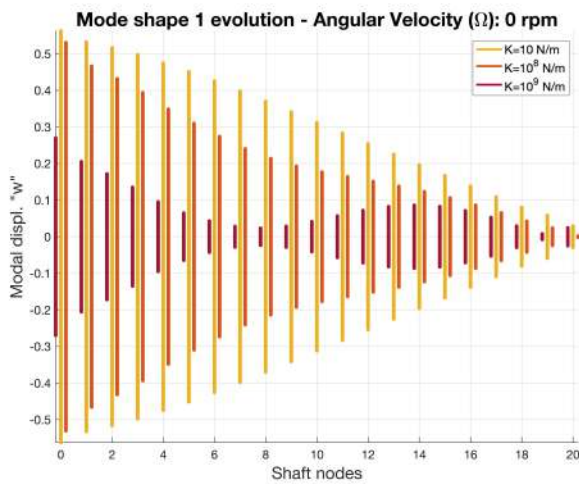


Figure 33: Combined mode shape 1

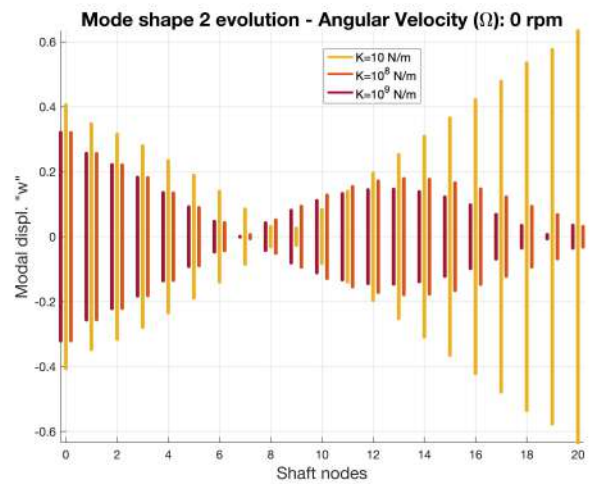


Figure 34: Combined mode shape 2

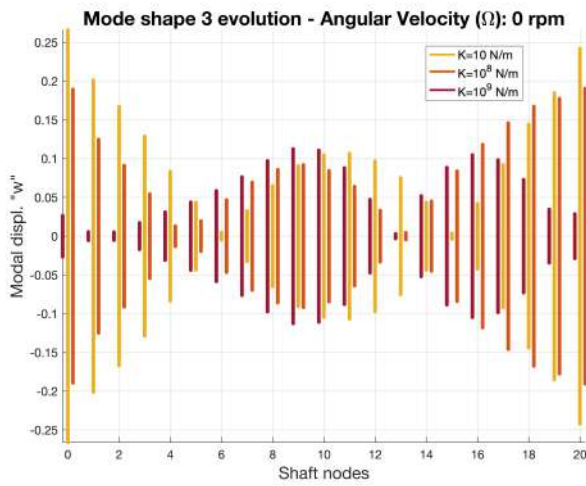


Figure 35: Combined mode shape 3

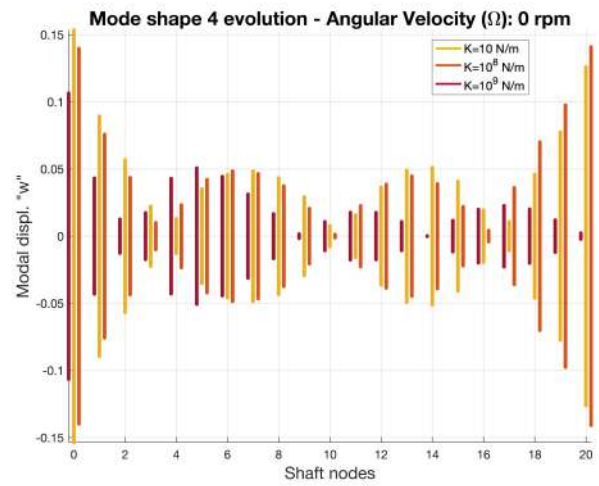


Figure 36: Combined mode shape 4

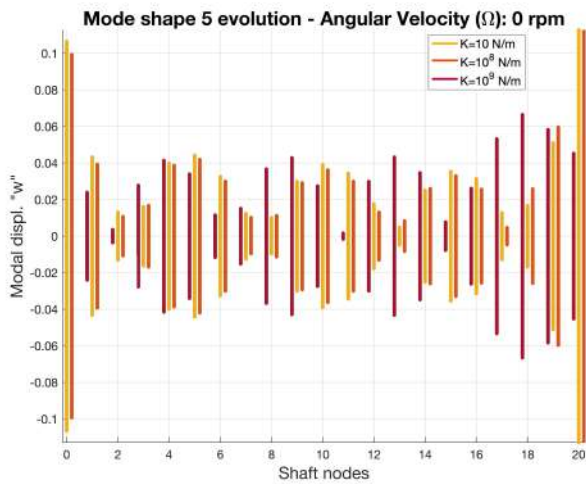


Figure 37: Combined mode shape 5

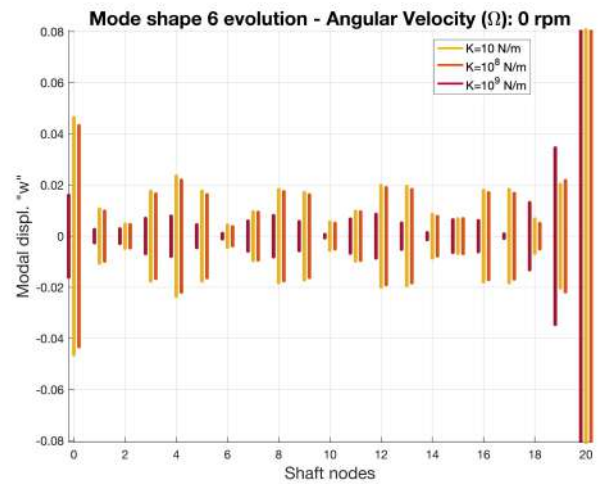


Figure 38: Combined mode shape 6

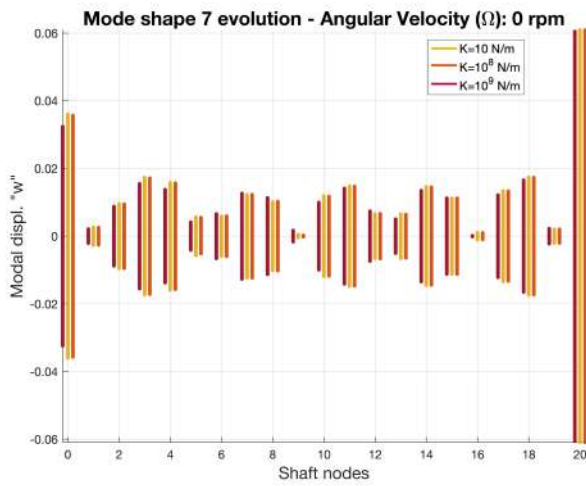


Figure 39: Combined mode shape 7

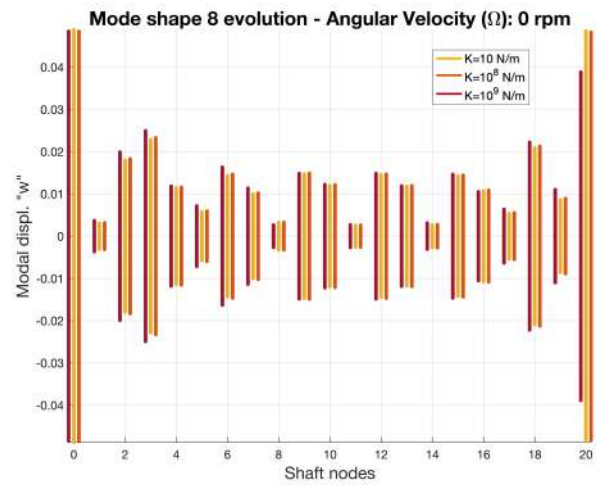
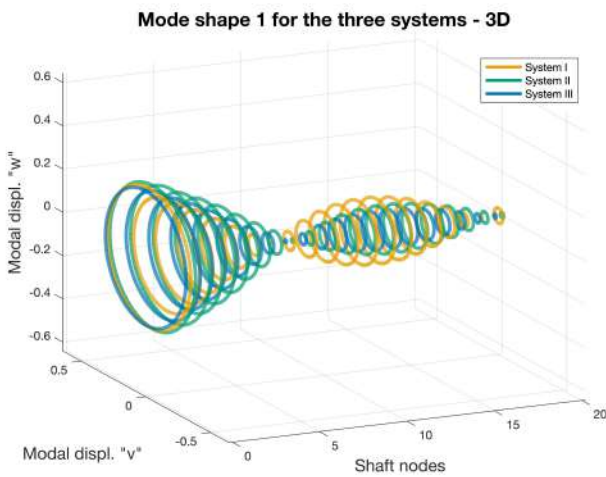
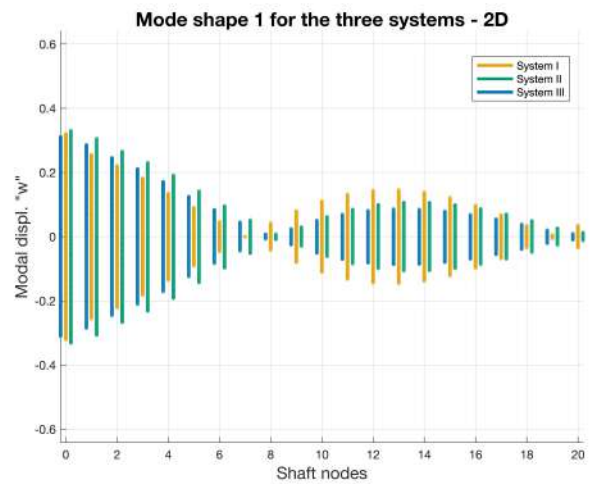
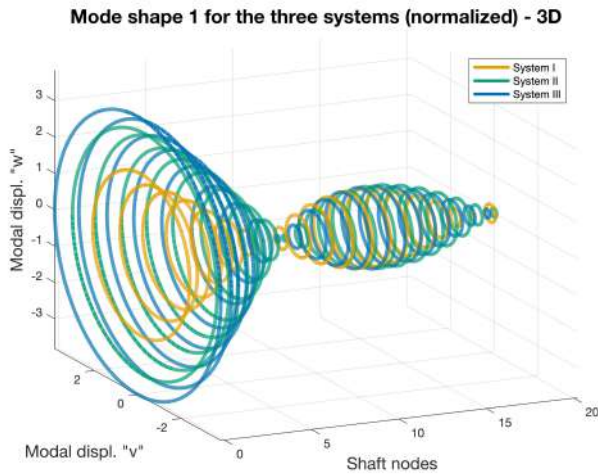
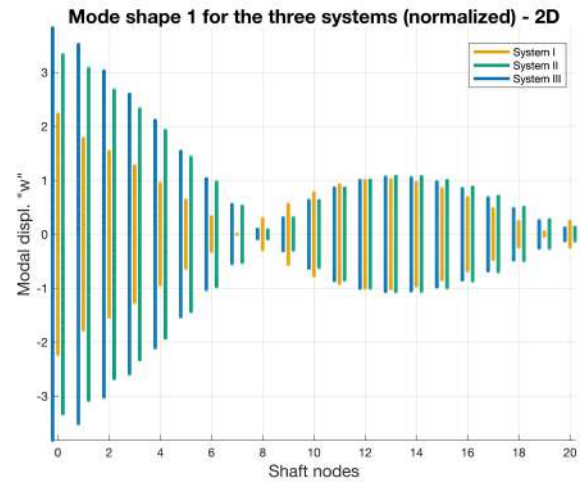


Figure 40: Combined mode shape 8

Figures 41 to 44 represent the mode shapes from section 3.2 complete of 2D and 3D representation. In the second set the amplitude is normalized with respect to the 13th node values.

Figure 41: 1st mode shape - 3DFigure 42: 1st mode shape - 2D

Figure 43: 1st normalized mode shape - 3DFigure 44: 1st normalized mode shape - 2D

Stiffness and damping evolution with speed for system II with hydrodynamic bearing as first bearing and ball bearing as last. A new set of graphs is presented in figures 45 and 46. In these graphs the influence of data interpolation is more evident.

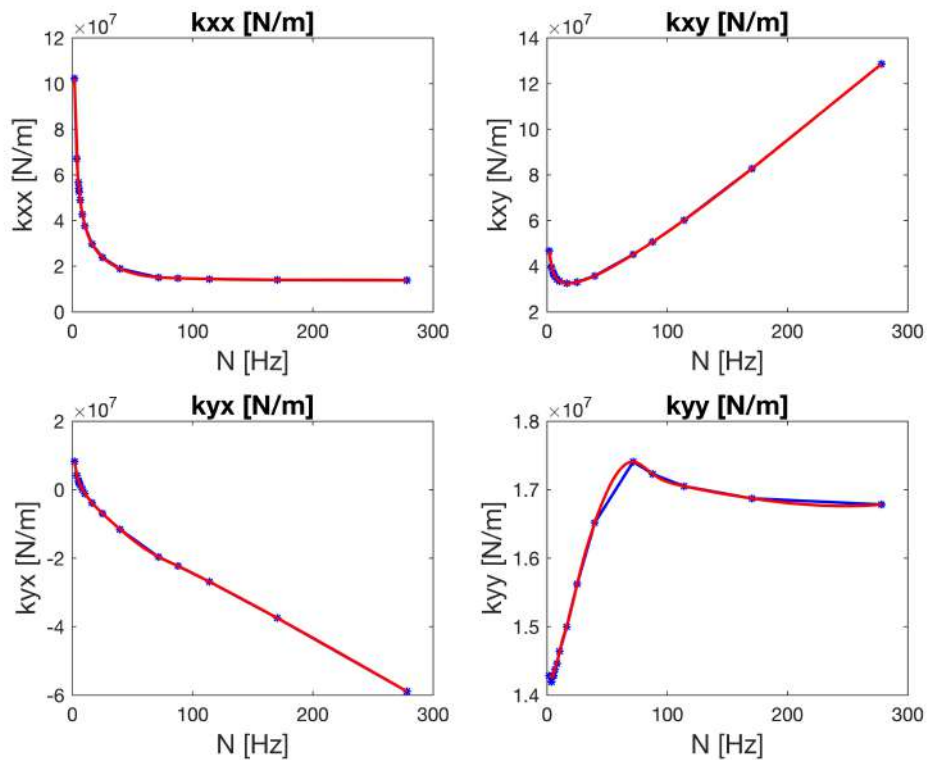


Figure 45: Stiffness evolution with speed

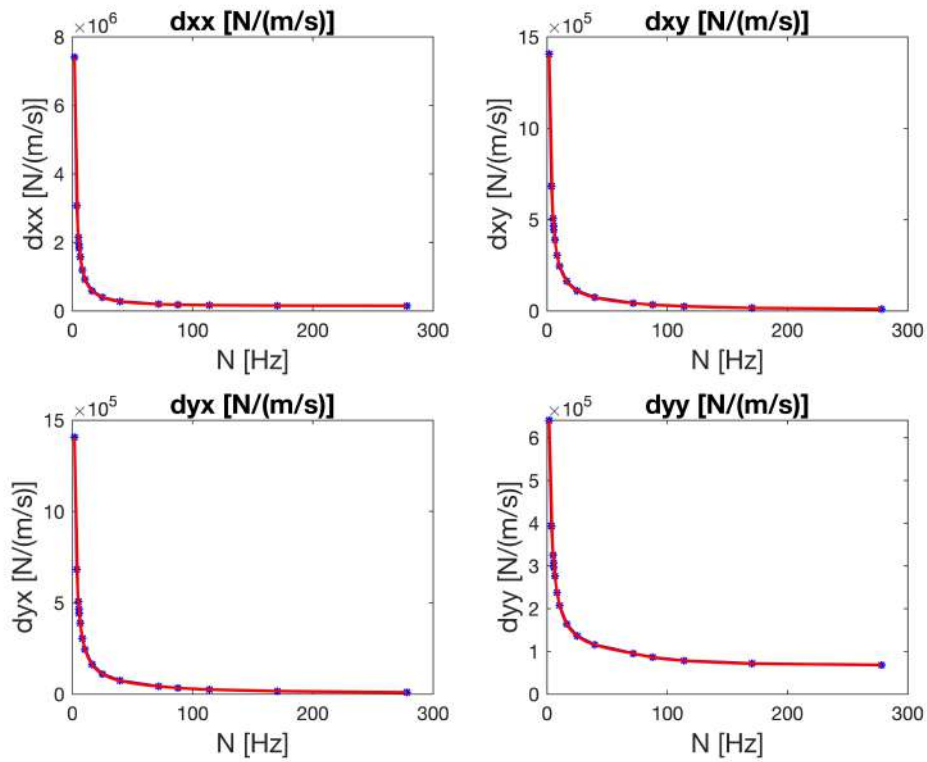


Figure 46: Damping evolution with speed

Appendix C - extended Campbell's diagram

Here the Campbell's diagram is extended including the second mode shape of the rotor system. In this second mode shape the difference between systems I and II is more evident, highlighting the effect of adding the second disk in terms of gyroscopic effect.

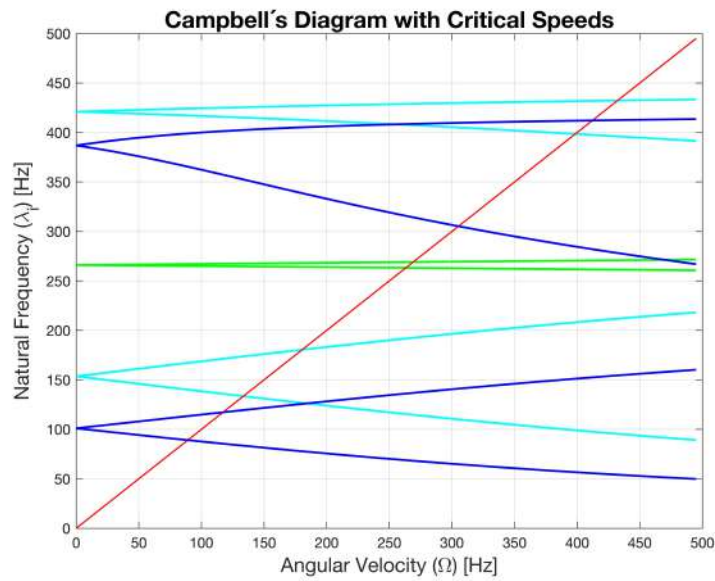


Figure 47: Campbell diagram extended

Appendix D - Shaft static equilibrium

Considering the volume of the disk, one can find the mass as $p_2 = 45.9\text{Kg}$. The equivalent point load on the shaft is $d_2 = 430.3\text{N}$. The shaft on the other hand weights 49.7Kg , yielding to a distributed load of $q = 423.9\text{N/m}$. With a length $L = 1150\text{mm}$ the calculations are presented in the system below (5.41) and load distributions are in figure 48.

$$\begin{cases} R_{y1} + R_{y2} = d_2 + qL \\ R_{x1} + R_{x2} = 0 \\ d_2 \cdot (0.355 - 0.190) + q \cdot (0.355 \cdot 0.355/2) - q \cdot (0.7315 \cdot 0.7315/2) \\ -q \cdot (0.0635 \cdot (0.0635/2 + 0.7315)) + R_{y2} \cdot 0.7315 = 0 \end{cases} \quad (5.41)$$

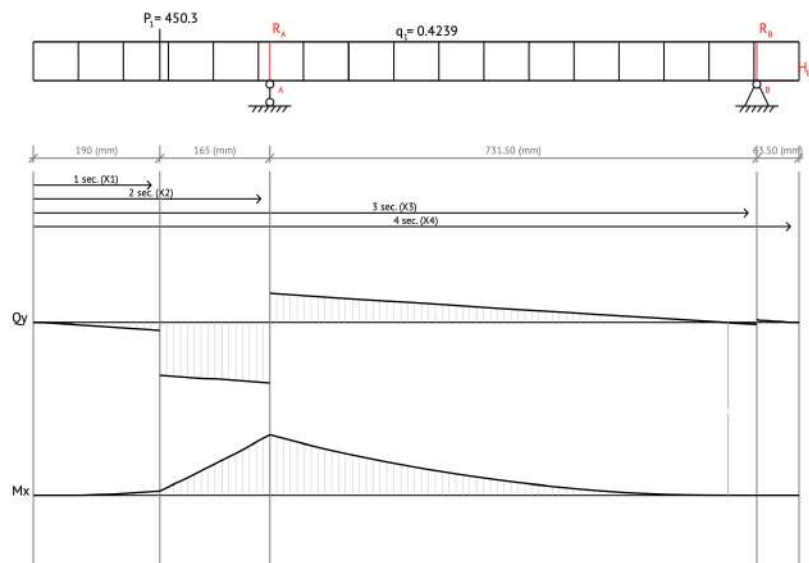


Figure 48: Static equilibrium of the shaft with diagrams

Yielding to R_{y1} and R_{y2} being equivalent to 892.7N and 45.0N. So finally $W_1 = 892.7\text{N}$ and $W_2 = 45.0\text{N}$.

Appendix E - Bearing data

The following table (8) illustrates the data available for the Two-axial-groove, $L/D = 0.5$, journal bearing employed in the project.

S	E	Φ	Q	P	T	K_{xx}	K_{xy}	K_{yx}	K_{yy}	B_{xx}	B_{xy}	B_{yx}	B_{yy}
6.430	0.071	81.89	0.121	0.860	5.7	1.55	14.41	-6.60	1.88	28.75	1.89	1.89	13.31
3.937	0.114	77.32	0.192	0.846	5.9	1.57	9.27	-4.20	1.89	18.44	1.93	1.93	8.58
2.634	0.165	72.36	0.271	0.833	6.2	1.61	6.74	-3.01	1.91	13.36	2.00	2.00	6.28
2.030	0.207	68.75	0.332	0.835	6.6	1.65	5.67	-2.50	1.93	11.18	2.07	2.07	5.33
1.656	0.244	65.85	0.383	0.835	7.0	1.69	5.06	-2.20	1.95	9.93	2.15	2.15	4.80
0.917	0.372	57.45	0.540	0.850	8.5	2.12	4.01	-1.30	1.85	7.70	2.06	2.06	3.23
0.580	0.477	51.01	0.651	0.900	10.5	2.67	3.70	-0.78	1.75	6.96	1.94	1.94	2.40
0.378	0.570	45.43	0.737	0.977	13.4	3.33	3.64	-0.43	1.68	6.76	1.87	1.87	1.89
0.244	0.655	40.25	0.804	1.096	17.9	4.21	3.74	-0.13	1.64	6.87	1.82	1.82	1.54
0.194	0.695	37.72	0.833	1.156	21.3	4.78	3.84	0.01	1.62	7.03	1.80	1.80	1.40
0.151	0.734	35.20	0.858	1.240	25.8	5.48	3.98	0.15	1.61	7.26	1.79	1.79	1.27
0.133	0.753	33.93	0.870	1.289	28.7	5.89	4.07	0.22	1.60	7.41	1.79	1.79	1.20
0.126	0.761	33.42	0.875	1.310	30.0	6.07	4.11	0.25	1.60	7.48	1.79	1.79	1.18
0.116	0.772	32.65	0.881	1.343	32.2	6.36	4.17	0.30	1.60	7.59	1.79	1.79	1.15
0.086	0.809	30.04	0.902	1.473	41.4	7.51	4.42	0.47	1.59	8.03	1.79	1.79	1.03
0.042	0.879	24.41	0.936	1.881	80.9	11.45	5.23	0.92	1.60	9.48	1.80	1.80	0.82

Table 8: Bearing data for Two-axial-groove, $L/D = 0.5$ journal bearing